

# Time-reversal symmetry-breaking charge order in a kagome superconductor

<https://doi.org/10.1038/s41586-021-04327-z>

Received: 25 June 2021

Accepted: 7 December 2021

Published online: 9 February 2022

 Check for updates

C. Mielke III<sup>1,2,17</sup>, D. Das<sup>1,17</sup>, J.-X. Yin<sup>3,17</sup>, H. Liu<sup>4,5,17</sup>, R. Gupta<sup>1</sup>, Y.-X. Jiang<sup>3</sup>, M. Medarde<sup>6</sup>, X. Wu<sup>7</sup>, H. C. Lei<sup>8</sup>, J. Chang<sup>2</sup>, Pengcheng Dai<sup>9</sup>, Q. Si<sup>9</sup>, H. Miao<sup>10</sup>, R. Thomale<sup>11,12</sup>, T. Neupert<sup>2</sup>, Y. Shi<sup>4,5,13</sup>, R. Khasanov<sup>1</sup>, M. Z. Hasan<sup>3,14,15,16</sup>✉, H. Luetkens<sup>1</sup> & Z. Guguchia<sup>1</sup>✉

The kagome lattice<sup>1</sup>, which is the most prominent structural motif in quantum physics, benefits from inherent non-trivial geometry so that it can host diverse quantum phases, ranging from spin-liquid phases, to topological matter, to intertwined orders<sup>2–8</sup> and, most rarely, to unconventional superconductivity<sup>6,9</sup>. Recently, charge sensitive probes have indicated that the kagome superconductors  $AV_3Sb_5$  ( $A = K, Rb, Cs$ )<sup>9–11</sup> exhibit unconventional chiral charge order<sup>12–19</sup>, which is analogous to the long-sought-after quantum order in the Haldane model<sup>20</sup> or Varma model<sup>21</sup>. However, direct evidence for the time-reversal symmetry breaking of the charge order remains elusive. Here we use muon spin relaxation to probe the kagome charge order and superconductivity in  $KV_3Sb_5$ . We observe a noticeable enhancement of the internal field width sensed by the muon ensemble, which takes place just below the charge ordering temperature and persists into the superconducting state. Notably, the muon spin relaxation rate below the charge ordering temperature is substantially enhanced by applying an external magnetic field. We further show the multigap nature of superconductivity in  $KV_3Sb_5$  and that the  $T_c/\lambda_{ab}^{-2}$  ratio (where  $T_c$  is the superconducting transition temperature and  $\lambda_{ab}$  is the magnetic penetration depth in the kagome plane) is comparable to those of unconventional high-temperature superconductors. Our results point to time-reversal symmetry-breaking charge order intertwining with unconventional superconductivity in the correlated kagome lattice.

The observation of orbital currents is a long-standing quest in both topological and correlated quantum matter. They have been suggested to produce the quantum anomalous Hall effect when interacting with Dirac fermions in a honeycomb lattice<sup>20</sup> (Fig. 1a) and to be the hidden phase of high-temperature cuprate superconductors<sup>21,22</sup> (Fig. 1b). In both cases, orbital currents run through the lattice and break time-reversal symmetry. Recently, the tantalizing visualization of such exotic order has been reported<sup>12–14</sup> in the kagome superconductors  $AV_3Sb_5$  ( $A = K, Rb, Cs$ ) (Fig. 1c). Scanning tunnelling microscopy observes a chiral  $2 \times 2$  charge order (Fig. 1d and Extended Data Figs. 1a–d and 2a–c) with an unusual magnetic field response. Theoretical analysis<sup>12–19</sup> also suggests that this chiral charge order can not only lead to a giant anomalous Hall effect<sup>23</sup> but can also be a precursor of unconventional superconductivity<sup>18</sup>. However, the broken time-reversal symmetry nature of the charge order and its interplay with superconductivity has not been explicitly demonstrated by experiments.

To explore unconventional aspects of superconductivity and the possible time-reversal symmetry-breaking nature of charge order and superconductivity in  $KV_3Sb_5$ , it is critical that the superconducting order parameter and weak internal fields of  $KV_3Sb_5$  are measured at the microscopic level. Thus, we concentrate on muon spin relaxation/rotation ( $\mu$ SR) experiments<sup>24</sup> of the normal state depolarization rate and the magnetic penetration depth  $\lambda$  in  $KV_3Sb_5$ . Importantly, zero-field  $\mu$ SR (ZF- $\mu$ SR) has the ability to detect internal magnetic fields as small as 0.1 G without applying external magnetic fields, making it a highly valuable tool for probing spontaneous magnetic fields owing to time-reversal symmetry breaking<sup>25</sup> in the superconducting and charge ordered states.

## Discussion

### Magnetic response across charge order

Although long-range magnetism has not been reported in  $KV_3Sb_5$  (ref. <sup>26</sup>), ZF- $\mu$ SR experiments have been carried out above and below

<sup>1</sup>Laboratory for Muon Spin Spectroscopy, Paul Scherrer Institute, Villigen PSI, Switzerland. <sup>2</sup>Physik-Institut, Universität Zürich, Winterthurerstrasse 190, Zürich, Switzerland. <sup>3</sup>Laboratory for Topological Quantum Matter and Advanced Spectroscopy (B7), Department of Physics, Princeton University, Princeton, NJ, USA. <sup>4</sup>Beijing National Laboratory for Condensed Matter Physics, Institute of Physics, Chinese Academy of Sciences, Beijing, China. <sup>5</sup>School of Physical Sciences, University of Chinese Academy of Sciences, Beijing, China. <sup>6</sup>Laboratory for Multiscale Materials Experiments, Paul Scherrer Institut, Villigen PSI, Switzerland. <sup>7</sup>Max-Planck-Institut für Festkörperforschung, Stuttgart, Germany. <sup>8</sup>Department of Physics and Beijing Key Laboratory of Opto-electronic Functional Materials and Micro-nano Devices, Renmin University of China, Beijing, China. <sup>9</sup>Department of Physics and Astronomy, Rice Center for Quantum Materials, Rice University, Houston, TX, USA. <sup>10</sup>Material Science and Technology Division, Oak Ridge National Laboratory, Oak Ridge, TN, USA. <sup>11</sup>Institut für Theoretische Physik und Astrophysik, Universität Würzburg, Würzburg, Germany. <sup>12</sup>Department of Physics, Indian Institute of Technology Madras, Chennai, India. <sup>13</sup>Songshan Lake Materials Laboratory, Dongguan, Guangdong, China. <sup>14</sup>Princeton Institute for the Science and Technology of Materials, Princeton University, Princeton, NJ, USA. <sup>15</sup>Materials Sciences Division, Lawrence Berkeley National Laboratory, Berkeley, CA, USA. <sup>16</sup>Quantum Science Center, Oak Ridge, TN, USA. <sup>17</sup>These authors contributed equally: C. Mielke III, D. Das, J.-X. Yin, H. Liu. ✉e-mail: mzhassan@princeton.edu; zurab.guguchia@psi.ch

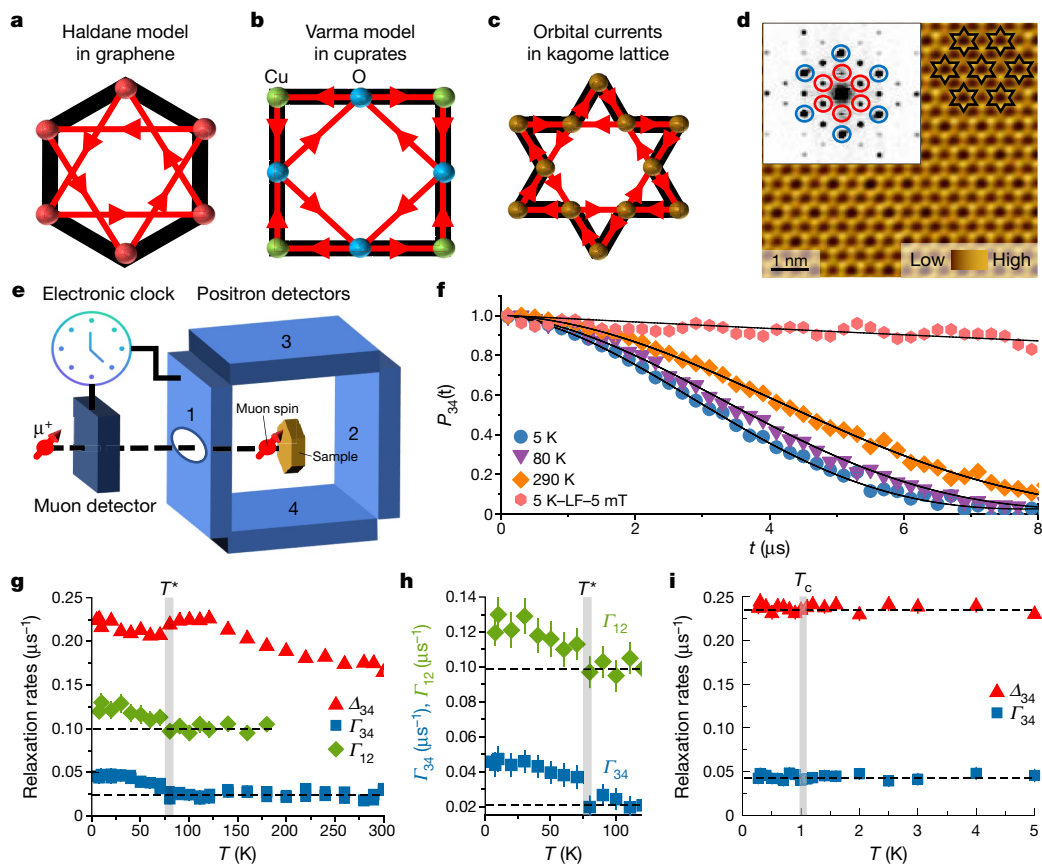


**Fig. 1 | Indication of time-reversal symmetry-breaking of the charge order in KV<sub>3</sub>Sb<sub>5</sub>.**

**a**, Orbital currents (red arrows) proposed in a honeycomb lattice. **b**, Orbital currents (red arrows) proposed in the CuO<sub>2</sub> lattice of cuprates. **c**, Schematic of orbital currents (red arrows) in the kagome lattice. **d**, Scanning tunnelling microscopy of the Sb surface showing 2 × 2 charge order as illustrated by the black lines. The inset is the Fourier transform of this image, showing lattice Bragg peaks marked by blue circles and 2 × 2 vector peaks marked by red circles. The three pairs of 2 × 2 vector peaks feature different intensities, denoting a chirality of the charge order. **e**, A schematic overview of the experimental setup. Spin polarized muons with spin S<sub>μ</sub>, forming at an angle of 60° with respect to the c axis of the crystal, are implanted in the sample. The sample was surrounded by four detectors: forwards (1), backwards (2), upwards (3) and downwards (4). An electronic clock is started at the time the

muon passes the muon detector and is stopped as soon as the decay positron is detected in the positron detectors. **f**, The ZF-μSR time spectra for KV<sub>3</sub>Sb<sub>5</sub>, obtained at different temperatures, all above the superconducting transition temperature T<sub>c</sub>. Longitudinally-applied field (LF) of 50 G clearly decouples the signal. The solid black curves in **a** represent fits to the recorded time spectra, using equation (1). Error bars are the s.e.m. in about 10<sup>6</sup> events. **g**, The temperature dependences of the relaxation rates Δ and Γ, obtained in a wide temperature range. **h**, The temperature dependence of Γ from two sets of detectors across the charge ordering temperature T\* ≈ 80 K. **i**, Temperature dependences of the muon spin relaxation rates Δ and Γ, which can be related to the nuclear and electronic systems, respectively, in the temperature range across T<sub>c</sub>. The error bars represent the s.d. of the fit parameters.

the superconducting transition temperature T<sub>c</sub> to search for any weak magnetism (static or slowly fluctuating). A schematic overview of the experimental setup with the muon spin forming at an angle of 60° with respect to the c axis of the crystal is shown in Fig. 1e. The sample was surrounded by four detectors: forwards (1), backwards (2), upwards (3) and downwards (4). Figure 1f displays the ZF-μSR spectra from detectors 3 and 4 collected over a wide temperature range. We see that the muon spin relaxation shows a reasonable temperature dependence. As the zero-field relaxation is decoupled by the application of a small external magnetic field applied in a direction longitudinal to the muon spin polarization, B<sub>LF</sub> = 50 G (Fig. 1f) (LF denotes “Longitudinal Field”), the relaxation is therefore due to spontaneous fields that are static at the microsecond timescale. The ZF-μSR spectra were fitted using the Gaussian Kubo–Toyabe (GKT) depolarization function<sup>27</sup>, which reflects the field distribution at the muon site created by the nuclear moments of the sample, multiplied by an additional exponential exp(−Γt) term (Extended Data Fig. 4a, b):

$$P_{ZF}^{GKT}(t) = \left( \frac{1}{3} + \frac{2}{3}(1 - \Delta^2 t^2) \exp\left[-\frac{\Delta^2 t^2}{2}\right] \right) \exp(-\Gamma t) \quad (1)$$

where Δ/γ<sub>μ</sub> is the width of the local field distribution due to the nuclear moments and γ<sub>μ</sub>/2π = 135.5 MHz T<sup>−1</sup> is the muon gyromagnetic ratio. The observed deviation from a pure GKT behaviour in paramagnetic systems is frequently seen in μSR measurements. This can, for example, be due to a mixture of diluted and dense nuclear moments, the presence of electric field gradients or a contribution of electronic origin. A GKT shape is expected due to the presence of the dense system of nuclear moments with large values of nuclear spins (I = 3/2 for <sup>39</sup>K, I = 7/2 for <sup>51</sup>V and I = 5/2 for <sup>121</sup>Sb) in KV<sub>3</sub>Sb<sub>5</sub> and a high natural abundance. The relaxation in single crystals might also not be GKT-like due to the fact that the quantization axis for the nuclear moments depends on the electric field gradients<sup>28</sup>. Naturally, the anisotropy of the electric field gradients is also often responsible for an anisotropy of the nuclear relaxation. As this effect essentially averages out in polycrystalline samples, we note that we also observed the additional exponential term in the polycrystalline sample of KV<sub>3</sub>Sb<sub>5</sub> (Extended Data Fig. 5a–c), which indicates that this effect is probably not dominant in our single-crystal measurements. Our high-field μSR results presented below, however, prove that there is indeed a strong contribution of electronic origin to the muon spin relaxation below the charge ordering temperature.

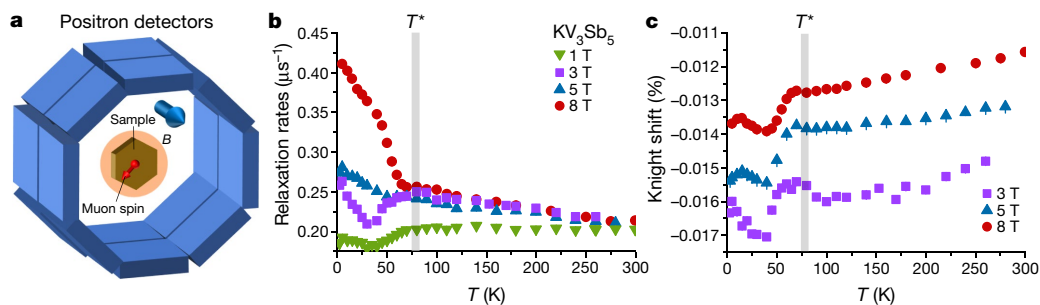


**Fig. 2 | Enhanced magnetic response of the charge order with applying external magnetic fields.** **a**, Schematic overview of the high-field  $\mu$ SR experimental setup for the muon spin forming an angle of  $90^\circ$  with respect to the  $c$  axis of the crystal. The sample was surrounded by  $2 \times 8$  positron detectors, arranged in rings. The specimen was mounted in a He gas-flow cryostat with the largest face perpendicular to the muon beam direction, along which the external field was applied. Behind the sample lies a veto counter (in orange),

Therefore, we conclude that  $\Gamma$  in zero magnetic field also tracks the temperature dependence of the electronic contribution, but we cannot exclude subtle effects owing to changes in the electric field gradients in the charge ordered state. In Fig. 1g, we see the temperature dependence of both the muon spin relaxation  $\Delta_{12}$  and  $\Gamma_{12,34}$  over a broad temperature range from the base temperature to 300 K. There is a notable increase immediately visible in the relaxation rates  $\Gamma_{12}$  and  $\Gamma_{34}$  on lowering the temperature below the charge ordering temperature  $T^*$ , which is more visible in Fig. 1h. This observation indicates the enhanced spread of internal fields sensed by the muon ensemble concurrent with the onset of charge ordering. The enhanced magnetic response that sets in with the charge order persists all the way down to the base temperature, and remains constant across the superconducting transition, as seen in Fig. 1i. Increase of the internal field width visible from the ZF- $\mu$ SR relaxation rate corresponds to an anomaly seen also in the nuclear contribution to the relaxation rate  $\Delta_{12}$ ; namely, a peak coincides with the onset of the charge order, which decreases to a broad minimum before increasing again towards lower temperatures.

The increase in the exponential relaxation below  $T^*$  is estimated to be  $\approx 0.025 \mu\text{s}^{-1}$ , which can be interpreted as a characteristic field strength of  $\Gamma_{12}/\gamma_\mu \approx 0.3$  G. We note that a similar value of internal magnetic field strength is reported in several time-reversal symmetry-breaking superconductors<sup>25</sup>. The dip-like temperature dependence of  $\Delta_{12}$  is also reminiscent of the behaviour observed in some multigap time-reversal symmetry-breaking superconductors (for example,  $\text{La}_7\text{Ni}_3$  (ref. 29)) across  $T_c$ . However, in the present case the ZF- $\mu$ SR results alone do not enable us to draw any conclusions on the time-reversal symmetry-breaking effect in  $\text{KV}_3\text{Sb}_5$  below  $T^*$ . As said above, the onset of charge order might also alter the electric field gradient experienced by the nuclei and correspondingly the magnetic dipolar coupling of the muon to the nuclei<sup>28</sup>. This can induce a change in the nuclear dipole contribution to the ZF- $\mu$ SR signal. To substantiate the above ZF- $\mu$ SR results, systematic high-field  $\mu$ SR<sup>30</sup> experiments are essential (Fig. 2a). In a high magnetic field, the direction of the applied field defines the quantization axis for the nuclear moments, so that the effect of the charge order on the electric field gradient at the nuclear sites is irrelevant. A non-monotonous behaviour of the relaxation rate is clearly seen in the  $\mu$ SR data, measured in a magnetic field of 1 T, applied parallel to the  $c$  axis, as shown in Fig. 2b. The data at 1 T look similar to the temperature dependence of the zero-field nuclear rate  $\Delta_{12}$ , as it seems to be dominated by the nuclear response. However, at higher fields such as 3 T, 5 T and 8 T, the rate not only shows a broad bump around  $T^*$ , but also shows a clear and stronger increase towards low temperatures in the charge ordered state, which is similar to the behaviour observed for the relaxation rates  $\Gamma_{12}$  and  $\Gamma_{34}$

which rejects the muons that do not hit the sample. **b, c**, The temperature dependence of the muon spin relaxation rate (**b**) and the Knight shift  $K_{\text{exp}}$  (local susceptibility) for  $\text{KV}_3\text{Sb}_5$  (**c**), measured under the  $c$ -axis magnetic fields of  $\mu_0 H = 1$  T, 3 T, 5 T and 8 T. The vertical grey lines mark the charge ordering temperature, determined from magnetization measurements (Methods).  $K_{\text{exp}}$  also shows a shallow minimum at around 30 K, followed by a small peak towards low temperatures. The error bars represent the s.d. of the fit parameters.

in zero field. As the nuclear contribution to the relaxation cannot be enhanced by an external field, this indicates that the low-temperature relaxation rate in magnetic fields higher than 1 T is dominated by the electronic contribution. Notably, we find that an absolute increase of the relaxation rate between the onset of charge order  $T^*$  and the base temperature in 8 T is  $0.15 \mu\text{s}^{-1}$ , which is a factor of six higher than that of  $0.025 \mu\text{s}^{-1}$  observed in zero field. This shows a strong field-induced enhancement of the electronic response. Moreover, we find that the magnitude of the Knight shift (local magnetic susceptibility), defined as  $K_{\text{exp}} = (B_{\text{int}} - B_{\text{ext}})/B_{\text{ext}}$  ( $B_{\text{int}}$  and  $B_{\text{ext}}$  (Extended Data Fig. 6) are the internally measured and externally applied magnetic fields, respectively) and obtained in 3 T, 5 T and 8 T shows a sharp increase just below  $T^*$ , as shown in Fig. 2c. The change in local magnetic susceptibility across the charge order temperature  $T^*$  agrees well with the change seen in the macroscopic susceptibility (Extended Data Fig. 3a, b) and indicates the presence of the magnetic response in  $\text{KV}_3\text{Sb}_5$  concurrent with the charge order.  $K_{\text{exp}}$  shows a shallow minimum near 30 K at 3 T, 5 T and 8 T, which is also seen in the macroscopic susceptibility. The minimum in  $K_{\text{exp}}$  is followed by a small peak towards low temperatures, which is absent in the macroscopic susceptibility. At present, it is difficult to give a quantitative explanation for the precise origin of such a behaviour. However, in connection with previous experimental results, one possibility is that the dip-like feature and the observed peak are related to the transition from isotropic charge order to a low-temperature electronic nematic state<sup>31,32</sup>, which breaks rotational symmetry. An electronic nematic transition in the charge ordered state was reported for the related system  $\text{CsV}_3\text{Sb}_5$  from transport<sup>31</sup> and scanning transmission microscope (STM) experiments<sup>32</sup>. The appearance of a nematic susceptibility would certainly influence the Knight shift and the muon spin relaxation rate. In addition, changes in the charge section will also modify the hyperfine contact field at the  $\mu^+$  site and therefore also the local susceptibility. If so, the modified local susceptibility will be reflected by a breakdown of the proportionality of the  $\mu^+$  Knight shift to the measured bulk susceptibility, because in this case the local susceptibility is different from the macroscopic susceptibility. This may explain the different temperature dependence of the muon Knight shift and macroscopic susceptibility in a charge ordered state.

The combination of ZF- $\mu$ SR and high-field  $\mu$ SR results shows the enhanced internal field width below  $T^*$ , giving direct evidence for the time-reversal symmetry-breaking fields in the kagome lattice. It is important to note that nearly the entire sample volume experiences an increase in the relaxation rate (Methods), indicating the bulk nature of the transition below  $T^*$ . Such an observation is consistent with charge sensitive probe results that show that the magnetic field switching of the chiral charge order is observed in the impurity-free region<sup>12</sup>.

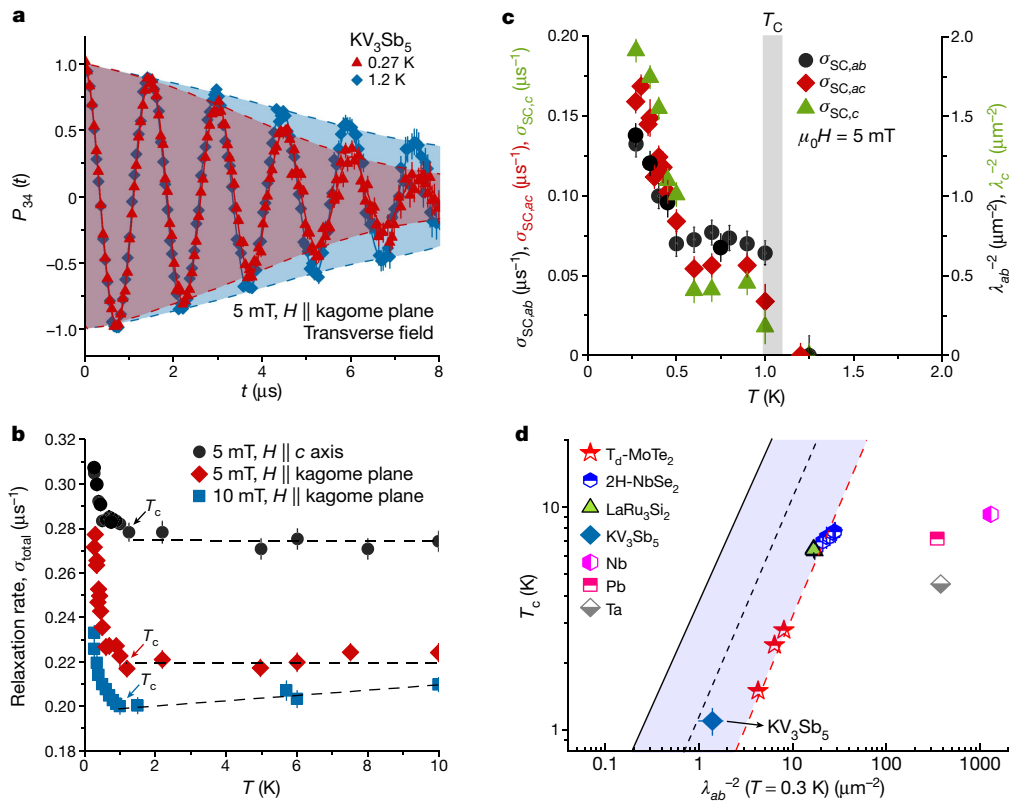


**Fig. 3 | Correlated kagome superconductivity.** **a**, The TF- $\mu$ SR spectra are obtained above and below  $T_c$  (after field cooling the sample from above  $T_c$ ). Error bars are the standard error of the mean in about  $10^6$  events. The error of each bin count  $n$  is given by the s.d. of  $n$ . The errors of each bin in  $A(t)$  are then calculated by standard error propagation. The solid lines in **a** represent fits to the data by means of equation (3). The dashed lines are a guide to the eye. **b**, The temperature dependence of the total muon spin relaxation rate  $\sigma_{\text{total}}$  measured in the magnetic fields of 5 mT and 10 mT applied both parallel to the  $c$  axis and parallel to the kagome plane. The dashed lines mark the average value of  $\sigma_{\text{total}}$  estimated from a few data points above  $T_c$ . **c**, The superconducting muon depolarization rates  $\sigma_{\text{SC},ab}$ ,  $\sigma_{\text{SC},ac}$  and  $\sigma_{\text{SC},c}$  as well as the

inverse squared magnetic penetration depth  $\lambda_{ab}^{-2}$  and  $\lambda_c^{-2}$  as a function of temperature, measured in 5 mT, applied parallel and perpendicular to the kagome plane. **d**, Plot of  $T_c$  versus  $\lambda_{ab}^{-2}(0)$  obtained from our  $\mu$ SR experiments in  $\text{KV}_3\text{Sb}_5$ . The dashed red line represents the relation obtained for the kagome superconductor  $\text{LaRu}_3\text{Si}_2$  and for the layered transition metal dichalcogenide superconductors  $\text{T}_d\text{-MoTe}_2$  and  $2\text{H-NbSe}_2$  (ref. <sup>38</sup>). The relation observed for underdoped cuprates is also shown (the solid line for hole doping<sup>37</sup> and the dashed black line for electron doping<sup>39,40</sup>). The points for various conventional BCS superconductors are also shown. The error bars represent the s.d. of the fit parameters.

Both the  $\mu$ SR and charge probe results attest to the intrinsic nature of the time-reversal symmetry breaking in the kagome lattice. One plausible phenomenological scenario is that the charge order has a complex chiral order parameter, which exhibits a phase difference between the three sublattices of the kagome plane. The existence of a phase difference, if not  $\pi$ , breaks time-reversal symmetry. Recent theoretical modelling of the charge ordering in the kagome lattice with van Hove filling and with extended Coulomb interactions (that is, close to the conditions of  $\text{AV}_3\text{Sb}_5$ ) also suggests that time-reversal symmetry-breaking charge order with orbital currents is energetically favourable<sup>16–19</sup>. The orbital currents do not break translation symmetry beyond the  $2 \times 2$  supercell of the charge order. In addition, at least according to the calculations<sup>16</sup>, the net flux in a  $2 \times 2$  unit cell of the charge order is vanishingly small. Hence, there is an extremely small net magnetic moment according to the theoretical modelling. The suggested orbital current was reported to be homogeneous on the lattice, however alternating in its flow, which would produce inhomogeneous fields at the muon site. In this framework, muons may couple to the closed current orbits below  $T_c$ , leading to an enhanced internal field width sensed by the muon ensemble concurrent with the charge order. Thus, we conclude that the present results provide key evidence for a time-reversal symmetry-breaking charge order in  $\text{KV}_3\text{Sb}_5$ . However, we cannot determine the exact structure of the orbital currents. Our data will inspire future experiments, particularly neutron

polarization analysis, to potentially understand the precise order of orbital currents in  $\text{KV}_3\text{Sb}_5$ . The current results indicate that the magnetic and charge channels of  $\text{KV}_3\text{Sb}_5$  seem to be strongly intertwined, which can give rise to complex and collective phenomena. The time-reversal symmetry-breaking charge order can open a topological gap in the Dirac nodal lines at the Fermi level, introducing a large anomalous Hall effect. It can also be a strong precursor of unconventional superconductivity as we show below.

### Unconventional superconductivity

The time-reversal symmetry-breaking charge order can arise from extended Coulomb interactions of the kagome lattice with van Hove singularities, in which the same interactions and instabilities can lead to correlated superconductivity. Thus, we next focus on the low transverse-field  $\mu$ SR (TF- $\mu$ SR) measurements performed in the superconducting state. With a superconducting transition temperature  $T_c$  of  $\approx 1.1$  K, the TF- $\mu$ SR spectra above (1.2 K) and below (0.27 K)  $T_c$  are shown in Fig. 3a. To obtain a well-ordered vortex lattice, the measurements were carried out after field cooling of the sample from above  $T_c$ . Above  $T_c$ , the oscillations show a damping essentially due to the random local fields from the nuclear magnetic moments. The damping rate is shown to be nearly constant between 10 K and 1.2 K. Below  $T_c$ , the damping rate increases with decreasing temperature due to the presence of a non-uniform local magnetic field distribution as a result of the

formation of a flux-line lattice in the superconducting state. Figure 3b depicts the temperature evolution of the total Gaussian relaxation rate  $\sigma_{\text{total}} = \sqrt{\sigma_{\text{SC}}^2 + \sigma_{\text{nm}}^2}$  for  $\text{KV}_3\text{Sb}_5$  for the 5 mT and 10 mT fields applied both in and out of the kagome plane. To extract the  $\sigma_{\text{SC}}$  contribution due only to superconductivity, the average value of the normal state depolarization rate  $\sigma_{\text{nm}}$ , estimated from six temperature points just above the onset of the superconducting transition, has been quadratically subtracted, because above  $T_c$  there is only the normal state contribution to  $\sigma_{\text{total}}$ . Figure 3c shows the temperature dependences of the superconducting relaxation rates  $\sigma_{\text{SC},ab}$  and  $\sigma_{\text{SC},ac}$ , determined from the data with the field applied along the  $c$  axis and in the kagome plane, respectively. The  $c$ -axis relaxation rate can be extracted as  $\sigma_{\text{SC},c} = \sigma_{\text{SC},ac}^2 / \sigma_{\text{SC},ab}$  (ref. <sup>33</sup>), which is shown as a function of temperature in Fig. 3c.

We note that the magnetic penetration depth  $\lambda(T)$  (right axis of Fig. 3c) is related to the relaxation rate  $\sigma_{\text{SC}}(T)$  in the presence of a triangular (or hexagonal) vortex lattice by the equation<sup>24</sup>:

$$\frac{\sigma_{\text{SC}}(T)}{\gamma_{\mu}} = 0.06091 \frac{\Phi_0}{\lambda^2(T)}, \quad (2)$$

where  $\gamma_{\mu}$  is the gyromagnetic ratio of the muon and  $\Phi_0$  is the magnetic-flux quantum. As the applied field is a factor of 20–60 times smaller than the second critical magnetic fields ( $\mu_0 H_{c2,c} \simeq 0.1$  T for  $H \parallel c$  and  $\mu_0 H_{c2,ab} \simeq 0.3$  T for  $H \parallel ab$ ) in  $\text{KV}_3\text{Sb}_5$ , equation (2) is valid to estimate both  $\lambda_{ab}$  and  $\lambda_c$ . The value of the in-plane penetration depth  $\lambda_{ab}$  at 0.3 K, determined from  $\sigma_{\text{SC},ab}$  (with superconducting screening currents flowing parallel to the kagome plane), is found to be  $\lambda_{ab} \simeq 877$  (+/-20) nm. The value of the out-of-plane penetration depth, determined from  $\sigma_{\text{SC},c}$  (with superconducting screening currents flowing perpendicular to the kagome plane), is found to be  $\lambda_c \simeq 730$  (+/-20) nm. The  $\lambda(T)$  in the applied field of 5 mT shows a well-pronounced two step behaviour, which is reminiscent of the behaviour observed in well-known two-band superconductors with single  $T_c$  such as  $\text{FeSe}_{0.94}$  (ref. <sup>33</sup>) and  $\text{V}_3\text{Si}$  (ref. <sup>34</sup>). These results were explained<sup>34</sup> by two nearly decoupled bands with an extremely weak interband coupling (which was still sufficient to give a single  $T_c$ ). According to our numerical analysis (Extended Data Figs. 7a–c and 8a–c) our observation of two-step behaviour of  $\lambda(T)$  in  $\text{KV}_3\text{Sb}_5$  is consistent with two-gap superconductivity with very weak interband coupling (0.001–0.005) and strong electron–phonon coupling. Multigap superconductivity was also recently reported for the sister compound  $\text{CsV}_3\text{Sb}_5$  by means of  $\mu\text{SR}$ <sup>35</sup> and  $\text{STM}$ <sup>36</sup>. The multigap superconductivity in  $\text{KV}_3\text{Sb}_5$  is consistent with the presence of multiple Fermi surfaces revealed by electronic structure calculations and tunnelling measurements<sup>14</sup>.

To place the system  $\text{KV}_3\text{Sb}_5$  in the context of other superconductors, in Fig. 3d we plot the critical temperature  $T_c$  against the superfluid density  $\lambda_{ab}^{-2}$ . Most unconventional superconductors have  $T_c/\lambda_{ab}^{-2}$  values of about 0.1–20, whereas all of the conventional Bardeen–Cooper–Schrieffer (BCS) superconductors lie on the far right in the plot, with much smaller ratios<sup>37</sup>. In other words, unconventional superconductors are characterized by a dilute superfluid (a low density of Cooper pairs) whereas conventional BCS superconductors exhibit a dense superfluid. Moreover, a linear relationship between  $T_c$  and  $\lambda_{ab}^{-2}$  is expected only on the Bose–Einstein–Condensate-like side of the phase diagram and is considered a hallmark of unconventional superconductivity<sup>37</sup>, in which (on-site or extended) Coulomb interactions play a role. For  $\text{KV}_3\text{Sb}_5$ , the ratio is estimated to be  $T_c/\lambda_{ab}^{-2} \simeq 0.7$ , which is far away from conventional BCS superconductors and approximately a factor of two greater than that of the charge-density-wave superconductors  $2\text{H-NbSe}_2$  and  $4\text{H-NbSe}_2$ , as well as the Weyl superconductor  $\text{Td-MoTe}_2$  (ref. <sup>38</sup>) and the kagome superconductor  $\text{LaRu}_3\text{Si}_2$ , as shown in Fig. 3d. The point for  $\text{KV}_3\text{Sb}_5$  is close to the values for electron-doped cuprates, which are well-known correlated superconductors with poorly screened Coulomb interactions.

## Conclusion

Our work points to a time-reversal symmetry-breaking charge order, intertwined with correlated superconductivity, in the kagome superconductor  $\text{KV}_3\text{Sb}_5$ . Although low-temperature time-reversal symmetry-breaking superconductivity has been discussed for many systems, high-temperature time-reversal symmetry-breaking charge order is extremely rare and there is a direct comparison with the fundamental Haldane and Varma models. The complex intertwining of such a charge ordered state with correlated superconductivity highlights the rich nature of the correlated kagome lattice and hints at other previously unknown hybrid phenomena resulting from non-trivial quantum interactions.

## Online content

Any methods, additional references, Nature Research reporting summaries, source data, extended data, supplementary information, acknowledgements, peer review information; details of author contributions and competing interests; and statements of data and code availability are available at <https://doi.org/10.1038/s41586-021-04327-z>.

1. Syözi, I. Statistics of kagome lattice. *Prog. Theor. Phys.* **6**, 306–308 (1951).
2. Barz, H. Ternary transition metal phosphides: high-temperature superconductors. *Mater. Res. Bull.* **15**, 1489–1491 (1980).
3. Zhou, Y., Kanoda, K. & Ng, T.-K. Quantum spin liquid states. *Rev. Mod. Phys.* **89**, 025003 (2017).
4. Guguchia, Z. et al. Tunable anomalous Hall conductivity through volume-wise magnetic competition in a topological kagome magnet. *Nat. Commun.* **11**, 559 (2020).
5. Yin, J.-X., Pan, S. H. & Hasan, M. Z. Probing topological quantum matter with scanning tunneling microscopy. *Nat. Rev. Phys.* **3**, 249–263 (2021).
6. Mielke, III, C. et al. Nodeless kagome superconductivity in  $\text{LaRu}_3\text{Si}_2$ . *Phys. Rev. Materials* **5**, 034803 (2021).
7. J.-X. Yin, et. al., Quantum-limit Chern topological magnetism in  $\text{TbMn}_6\text{Sn}_6$ . *Nature* **583**, 533–536 (2020).
8. Pershoguba, S. S. & Yakovenko, V. M. Optical control of topological memory based on orbital magnetization. Preprint at <http://arxiv.org/abs/2106.01192> (2021).
9. Ortiz, B. et al.  $\text{CsV}_3\text{Sb}_5$ : a  $Z_2$  topological kagome metal with a superconducting ground state. *Phys. Rev. Lett.* **125**, 247002 (2020).
10. Ortiz, B. et al. Superconductivity in the  $Z_2$  kagome metal  $\text{KV}_3\text{Sb}_5$ . *Phys. Rev. Materials* **5**, 034801 (2021).
11. Yin, Q. et al. Superconductivity and normal-state properties of kagome metal  $\text{RbV}_3\text{Sb}_5$  single crystals. *Chin. Phys. Lett.* **38**, 037403 (2021).
12. Jiang, Y.-X. et al. Discovery of topological charge order in kagome superconductor  $\text{KV}_3\text{Sb}_5$ . *Nat. Mater.* **20**, 1353–1357 (2021).
13. Shumiya, N. et al. Tunable chiral charge order in kagome superconductor  $\text{RbV}_3\text{Sb}_5$ . *Phys. Rev. B* **104**, 035131 (2021).
14. Wang, Z. et al. Electronic nature of chiral charge order in the kagome superconductor  $\text{CsV}_3\text{Sb}_5$ . *Phys. Rev. B* **104**, 075148 (2021).
15. Feng, X., Jiang, K., Wang, Z. & Hu, J. Chiral flux phase in the Kagome superconductor  $\text{AV}_3\text{Sb}_5$ . *Sci. Bull.* **66**, 1384–1388 (2021).
16. Denner, M., Thomale, R. & Neupert, T. Analysis of charge order in the kagome metal  $\text{AV}_3\text{Sb}_5$  ( $A = \text{K, Rb, Cs}$ ). *Phys. Rev. Lett.* **127**, 217601 (2021).
17. Lin, Y.-P. & Nandkishore, R. Complex charge density waves at Van Hove singularity on hexagonal lattices: Haldane-model phase diagram and potential realization in kagome metals  $\text{AV}_3\text{Sb}_5$ . *Phys. Rev. B* **104**, 045122 (2021).
18. Wu, X. et al. Nature of unconventional pairing in the kagome superconductors  $\text{AV}_3\text{Sb}_5$ . *Phys. Rev. Lett.* **127**, 177001 (2021).
19. Setty, C., Hu, H., Chen, L. & Si, Q. Electron correlations and  $T$ -breaking density wave order in a  $Z_2$  kagome metal. Preprint at <https://arxiv.org/abs/2105.15204> (2021).
20. Haldane, F. D. M. Model for a quantum Hall effect without Landau levels: condensed-matter realization of the parity anomaly. *Phys. Rev. Lett.* **61**, 2015–2018 (1988).
21. Varma, C. M. Non-Fermi-liquid states and pairing instability of a general model of copper oxide metals. *Phys. Rev. B* **55**, 14554–14580 (1997).
22. Chakravarty, S., Laughlin, R., Morr, D. & Nayak, C. Hidden order in the cuprates. *Phys. Rev. B* **63**, 094503 (2001).
23. Yang, S. et al. Giant, unconventional anomalous Hall effect in the metallic frustrated magnet candidate,  $\text{KV}_3\text{Sb}_5$ . *Sci. Adv.* **6**, eabb6003 (2020).
24. Sonier, J. E., Brewer, J. H. & Kiefl, R. F.  $\mu\text{SR}$  studies of the vortex state in type-II superconductors. *Rev. Mod. Phys.* **72**, 769 (2000).
25. Luke, G. M. et al. Time-reversal symmetry breaking superconductivity in  $\text{Sr}_2\text{RuO}_4$ . *Nature* **394**, 558–561 (1998).
26. Kenney, E., Ortiz, B., Wang, C., Wilson, S. & Graf, M. Absence of local moments in the kagome metal  $\text{KV}_3\text{Sb}_5$  as determined by muon spin spectroscopy. *J. Phys. Condens. Matter* **33**, 235801 (2021).
27. Kubo, R. & Toyabe, T. *Magnetic Resonance and Relaxation* (North Holland, 1967).
28. Huang, W. et al. Precision search for magnetic order in the pseudogap regime of  $\text{La}_{2-x}\text{Sr}_x\text{CuO}_4$  by muon spin relaxation. *Phys. Rev. B* **85**, 104527 (2012).

29. Singh, A. D. et al. Time-reversal symmetry breaking and multigap superconductivity in the noncentrosymmetric superconductor  $\text{La}_7\text{Ni}_3$ . *Phys. Rev. B* **103**, 174502 (2021).
30. Sedlak, K., Scheuermann, R., Stoykov, A. & Amato, A. GEANT4 simulation and optimisation of the high-field  $\mu\text{SR}$  spectrometer. *Physica B* **404**, 970–973 (2009).
31. Xiang, Y. et al. Twofold symmetry of c-axis resistivity in topological kagome superconductor  $\text{CsV}_3\text{Sb}_5$  with in-plane rotating magnetic field. Preprint at <https://arxiv.org/abs/2104.06909> (2021).
32. Zhao, H. et al. Cascade of correlated electron states in a kagome superconductor  $\text{CsV}_3\text{Sb}_5$ . Preprint at <https://arxiv.org/pdf/2103.03118> (2021).
33. Khasanov, R. et al. Evolution of two-gap behavior of the superconductor  $\text{FeSe}_{1-x}$ . *Phys. Rev. Lett.* **104**, 087004 (2010).
34. Kogan, V. G., Martin, C. & Prozorov, R. Superfluid density and specific heat within a self-consistent scheme for a two-band superconductor. *Phys. Rev. B* **80**, 014507 (2009).
35. Gupta, R. et al. Microscopic evidence for anisotropic multigap superconductivity in the  $\text{CsV}_3\text{Sb}_5$  kagome superconductor. Preprint at <https://arxiv.org/abs/2108.01574> (2021).
36. Han-Shu, X. et al. Multiband superconductivity with sign-preserving order parameter in kagome superconductor  $\text{CsV}_3\text{Sb}_5$ . Preprint at <https://arxiv.org/pdf/2104.08810.pdf> (2021).
37. Uemura, Y. J. et al. Universal correlations between  $T_c$  and  $n_s/m^*$  (carrier density over effective mass) in high- $T_c$  cuprate superconductors. *Phys. Rev. Lett.* **62**, 2317 (1989).
38. von Rohr, F. O. et al. Unconventional scaling of the superfluid density with the critical temperature in transition metal dichalcogenides. *Sci. Adv.* **5**, eaav8465 (2019).
39. Shengelaya, A. et al. Muon-spin-rotation measurements of the penetration depth of the infinite-layer electron-doped  $\text{Sr}_{0.9}\text{La}_{0.1}\text{CuO}_2$  cuprate superconductor. *Phys. Rev. Lett.* **94**, 127001 (2005).
40. Luetkens, H. et al. The electronic phase diagram of the  $\text{LaO}_{1-x}\text{F}_x\text{FeAs}$  superconductor. *Nat. Mater.* **8**, 305–309 (2009).

**Publisher's note** Springer Nature remains neutral with regard to jurisdictional claims in published maps and institutional affiliations.

© The Author(s), under exclusive licence to Springer Nature Limited 2022

## Methods

### Sample preparation

Single crystals of  $KV_3Sb_5$  were grown from  $KSb_2$  alloy as a flux. K, V and Sb elements and  $KSb_2$  precursor were sealed in a Ta crucible in a molar ratio of 1:3:14:10, which was finally sealed in a highly evacuated quartz tube. The tube was heated up to 1,273 K, left for 20 h and then slowly cooled down to 773 K. Single crystals were separated from the flux by centrifuging. The crystals obtained from the flux were thin, metallic platelets with high lustre and the largest size was approximately  $5 \times 5 \text{ mm}^2$ . The obtained crystals with natural hexagonal facets were easily exfoliated. The X-ray diffraction pattern of a single crystal of  $KV_3Sb_5$  was collected using a Bruker D2 Phaser X-ray diffractometer with Cu  $K\alpha$  radiation ( $\lambda = 0.15418 \text{ nm}$ ) at room temperature. The single-crystal diffraction was implemented on a Bruker D8 Venture system equipped with Mo  $K\alpha$  radiation ( $\lambda = 0.71073 \text{ \AA}$ ). The crystal structure was solved and refined using the Bruker SHELXTL software package. Critical magnetic fields for  $KV_3Sb_5$  for the field applied along the  $c$  axis and in the kagome plane were 100 mT and 300 mT, respectively.

### Experimental details

ZF- and TF- $\mu$ SR experiments on the single-crystalline samples of  $KV_3Sb_5$  were performed on the GPS, Dolly and high-field HAL-9500 instruments at the Swiss Muon Source ( $S\mu S$ ) at the Paul Scherrer Institute, in Villigen, Switzerland. Zero field is dynamically obtained (compensation better than 30 mG) by a newly installed automatic compensation device<sup>41</sup>. When performing measurements in zero field the geomagnetic field or any stray fields are tabulated and automatically compensated for by the automatic compensation device.

Because the  $KV_3Sb_5$  samples were thin (0.13–0.35 mm along the  $c$  axis), a mosaic of several crystals stacked on top of each other was used for these measurements. The individual crystals were attached to a 25- $\mu\text{m}$ -thick Cu foil mounted on the Cu sample fork, and the entire ensemble was held together by small droplets of GE varnish. The crystals were aligned with the same in-plane orientation, which was achievable because the thin sheet-like crystals grow with a clearly hexagonal shape (Extended Data Fig. 1c). These multilayer crystal mosaics were then wrapped in a single layer of 60  $\mu\text{m}$  PE polyester tape. The magnetic field was applied both in-plane (along the  $ab$  plane) and out-of-plane (along the crystallographic  $c$  axis). A schematic overview of the experimental setup for zero-field and low-transverse-field measurements in GPS is shown in Fig. 1a. The muon spin forms at an angle of  $60^\circ$  with respect to the  $c$  axis of the crystal. The sample was surrounded by four detectors. A schematic overview of the experimental setup for the high-field  $\mu$ SR instrument is shown in Fig. 2a. The crystals were mounted on 10 mm circular silver sample holder by small droplets of GE varnish. The muon spin forms at an angle of  $90^\circ$  with respect to the  $c$  axis of the crystal. The sample was surrounded by  $2 \times 8$  positron detectors, arranged in rings. The specimen was mounted in a He gas-flow cryostat with the largest face perpendicular to the muon beam direction, along which the external field was applied.

### $\mu$ SR experiment

In a  $\mu$ SR experiment, nearly 100% spin-polarized muons  $\mu^+$  are implanted into the sample one at a time. The positively charged  $\mu^+$  thermalize at interstitial lattice sites, where they act as magnetic microprobes. In a magnetic material the muon spin precesses in the local field  $B_{\text{int}}$  at the muon site with the Larmor frequency  $\nu_{\text{int}} = \gamma_{\mu}/(2\pi)B_{\text{int}}$  (muon gyromagnetic ratio  $\gamma_{\mu}/(2\pi) = 135.5 \text{ MHz T}^{-1}$ ). Using the  $\mu$ SR technique, important length scales of superconductors can be measured, namely the magnetic penetration depth  $\lambda$  and the coherence length  $\xi$ . If a type II superconductor is cooled below  $T_c$  in an applied magnetic field ranging between the lower ( $H_{c1}$ ) and the upper ( $H_{c2}$ ) critical fields, a vortex lattice is formed that in general is incommensurate with the crystal lattice, with vortex cores separated by much larger distances than

those of the crystallographic unit cell. Because the implanted muons stop at the given crystallographic sites, they will randomly probe the field distribution of the vortex lattice. Such measurements need to be performed in a field applied perpendicular to the initial muon spin polarization (the so-called transverse-field configuration).  $\lambda$  is one of the fundamental parameters of a superconductor, as it is related to the superfluid density  $n_s$  via  $1/\lambda^2 = \mu_0 e^2 n_s / m^*$  (where  $m^*$  is the effective mass,  $e$  is the elementary charge and  $\mu_0$  is the Bohr magneton).

### Analysis of TF- $\mu$ SR data

The TF- $\mu$ SR data were analysed by using the following functional form<sup>42</sup>:

$$P_{\text{TF}}(t) = A_s \exp\left[-\frac{(\sigma_{\text{SC}}^2 + \sigma_{\text{nm}}^2)t^2}{2}\right] \cos(\gamma_{\mu} B_{\text{int},s} t + \varphi) \quad (3)$$

Here  $A_s$  denotes the initial asymmetry of the sample,  $\varphi$  is the initial phase of the muon-spin ensemble and  $B_{\text{int}}$  represents the internal magnetic field at the muon site. The relaxation rates  $\sigma_{\text{SC}}$  and  $\sigma_{\text{nm}}$  characterize the damping due to the formation of the flux-line lattice in the superconducting state and of the nuclear magnetic dipolar contribution, respectively. As indicated by the solid line in Fig. 3a, the  $\mu$ SR data are well described by equation (1).

### Crystal structure of $KV_3Sb_5$

Additional characterization information is provided here on the kagome superconductor  $KV_3Sb_5$ , which crystallizes in the new  $AV_3Sb_5$ -type structure (space group  $P6/mmm$ , where  $A = \text{K, Rb, Cs}$ ). The crystallographic structure of prototype compound  $KV_3Sb_5$  shown in panel a of Extended Data Fig. 1 illustrates how the V atoms form a kagome lattice (medium beige circles) intertwined with a hexagonal lattice of Sb atoms (small red circles). The K atoms (large purple circles) occupy the interstitial sites between the two parallel kagome planes. In panel b the vanadium kagome net has been emphasized, with the interpenetrating antimony lattice included to highlight the unit cell (see dashed lines). Extended Data Figure 1c, d shows an optical microscope image of a  $3 \times 2 \times 0.2 \text{ mm}^3$  single crystal of  $KV_3Sb_5$  on millimetre paper and an STM image of the V kagome lattice from a cryogenically cleaved sample, respectively.

### Extended laboratory X-ray diffraction experiments of $KV_3Sb_5$

A single-crystalline sample was selected and X-ray diffraction was performed on it. The crystal was oriented such that the incident X-rays scattered off of the  $ab$  plane. The resultant diffraction pattern shows clear diffraction peaks, which have been indexed (Extended Data Fig. 2a) and fitted using the SHELX-2018/3 software program. The obtained crystallographic information is summarized in Extended Data Tables 1 and 2. The Laue X-ray diffraction image (Extended Data Fig. 2b) demonstrates the single crystallinity of the samples used for the  $\mu$ SR experiments.

### Extended magnetic susceptibility measurements of $KV_3Sb_5$

The magnetic susceptibility measurements show the abrupt drop in susceptibility at  $T \approx 80 \text{ K}$  (Extended Data Fig. 2c), which comes from the charge ordering below this temperature. Such an anomaly in susceptibility across the charge order  $T$  is seen up to the highest magnetic field applied along the  $c$  axis (Extended Data Fig. 3a). Interestingly, a shallow minimum around 30 K is also seen in the macroscopic susceptibility similar to  $\mu$ SR Knight shift data. Whether this increase is related to the appearance of the electronic nematic susceptibility or not is an open question and requires more exploration. Notably, the anomaly in magnetic susceptibility across the charge order temperature  $T$  is very well pronounced when the field is applied along the  $c$  axis, whereas it is hardly seen when the field is applied along the kagome plane (Extended Data Fig. 3b). This indicates that the magnetic response across  $T$  is anisotropic. We note that the field dependence of the charge order peak intensities, observed with STM, is also seen only when the magnetic field

is applied along the  $c$  axis, pointing to the anisotropic field response of a charge order. These results are consistent with the scenario of orbital currents: as the orbital currents are coupled to the  $c$ -axis moment and do not produce in-plane fields, the pronounced change in susceptibility is seen only when field is applied along the  $c$  axis.

We note that the temperature dependence of the  $\mu$ SR Knight shift,  $K_{\text{exp}}$ , towards the low temperatures in the charge ordered state does not fully coincide with the temperature dependence of the macroscopic susceptibility; for example, the peak that was seen in  $K_{\text{exp}}$  near 15 K is missing in the macroscopic susceptibility. We note that in a paramagnetic metal  $K_{\text{exp}}$  originates from hyperfine fields produced by the field-induced polarization of conduction electrons and localized electronic moments. The local moments contribute to  $K_{\text{exp}}$  through two coupling mechanisms: (1) the dipolar interaction between the local moments and the  $\mu^+$ , which may be described as a dipolar field at the  $\mu^+$  interstitial site, and (2) a contact term due to electron spin polarization at the interstitial  $\mu^+$ . Both contributions are proportional to the local-moment susceptibility. As there is a possible transition from isotropic charge order to a nematic state in  $\text{KV}_3\text{Sb}_5$  below 30 K, changes in the charge section will modify a hyperfine contact field and therefore also the local susceptibility. This may explain the different temperature dependence of the muon Knight shift and the macroscopic susceptibility in the charge ordered state.

## ZF- $\mu$ SR spectrum for $\text{KV}_3\text{Sb}_5$

The ZF- $\mu$ SR spectrum recorded at 5 K is displayed in Extended Data Fig. 4. The red solid curve represents the fit to the recorded time spectra, using only the GKT function<sup>27</sup>:

$$P_{\text{ZF}}^{\text{GKT}}(t) = \left( \frac{1}{3} + \frac{2}{3}(1 - \Delta^2 t^2) \exp\left[-\frac{\Delta^2 t^2}{2}\right] \right) \quad (4)$$

where  $\Delta/\gamma_\mu$  is the width of the local field distribution due to the nuclear moments and  $\gamma_\mu/2\pi = 135.5 \text{ MHz T}^{-1}$  is the muon gyromagnetic ratio. The GKT depolarization function (equation (1)) reflects the field distribution at the muon site created by the nuclear moments of the sample. It is clear that the GKT function alone is not sufficient to fully describe the ZF- $\mu$ SR spectrum. Multiplying the GKT function by the additional exponential  $\exp(-\Gamma t)$  term (equation (1)), which is of electronic in origin, is essential to fully describe the spectrum shown in Extended Data Fig. 4a and in the inset. Thus, ZF- $\mu$ SR consists of the muon spin relaxations  $\Delta$  and  $\Gamma$  due to the nuclear and electronic moments, respectively. This additional exponential rate is higher in the spectra taken from the forwards and backwards detectors as shown in Extended Data Fig. 4b.

## ZF- $\mu$ SR results for the polycrystalline sample of $\text{KV}_3\text{Sb}_5$

We carried out ZF- $\mu$ SR experiments on the polycrystalline sample of  $\text{KV}_3\text{Sb}_5$  and the results are shown in Extended Data Fig. 5. The additional exponential term is clearly visible in the spectrum as shown in Extended Data Fig. 5a and in the inset, showing the early time behaviour. There is a clear increase immediately visible in the exponential relaxation rate upon lowering the temperature below the charge ordering temperature  $T^*$  (Extended Data Fig. 5b), which is more visible in Extended Data Fig. 5c. This observation in the polycrystalline sample of  $\text{KV}_3\text{Sb}_5$  agrees very well with the results on the single crystals. Our results on several  $\text{KV}_3\text{Sb}_5$  samples (both in single crystals and polycrystals) indicate that the exponential term is intrinsically present and is enhanced below  $T^*$ .

## High-field $\mu$ SR spectrum for a single crystal of $\text{KV}_3\text{Sb}_5$

During the high-field experiments obtained on the instrument HAL-9500, a mosaic of several crystals stacked on top of each other was used. The individual crystals were attached to a 10 mm circular silver sample holder and the entire ensemble was held together by small droplets of GE varnish. Extended Data Figure 6 shows the probability

field distribution, measured at 5 K in the  $c$ -axis magnetic field of 8 T. In the whole investigated temperature range, two-component signals were observed: a signal with fast relaxation of  $0.42 \mu\text{s}^{-1}$  (broad signal) and another one with a slow relaxation of  $0.08 \mu\text{s}^{-1}$  (narrow signal). The narrow signal arises mostly from the muons stopping in the silver sample holder and its position is a precise measure of the value of the applied magnetic field. The width and the position of the narrow signal are found to be temperature independent (see the inset of Extended Data Fig. 6) as expected and thus they were kept constant in the analysis. The relative fraction of the muons stopping in the sample was fixed to the value obtained at the base temperature and kept temperature independent. The signal with the fast relaxation, which is shifted towards the lower field from the applied one, arises from the muons stopping in the sample and it takes a major fraction (60–70%) of the  $\mu$ SR signal. This points to the fact that the sample response arises from the bulk of the sample. Based on this two-component signal, we can determine the Knight shift, which is defined as  $K_{\text{exp}} = (B_{\text{int}} - B_{\text{ext}})/B_{\text{ext}}$ , where  $B_{\text{int}}$  and  $B_{\text{ext}}$  are the internal and externally applied magnetic fields, respectively.

## Superconducting gap symmetry

Theoretically, several scenarios for electronically mediated, unconventional superconductivity have been discussed<sup>18</sup>. In the band structure of the  $\text{AV}_3\text{Sb}_5$  materials, van Hove singularities are found close to the Fermi energy, which is an electronic structural motif shared with other systems such as the cuprate superconductors or  $\text{Sr}_2\text{RuO}_4$ . As a particular feature of the kagome lattice, however, there is a sublattice interference mechanism<sup>43</sup> by which the Bloch states near each van Hove point are supported on a distinct sublattice. This promotes the relevance of longer-range interactions and unconventional pairing states.

Extended Data Figure 7a shows the temperature dependences of the superconducting relaxation rates  $\sigma_{\text{SC},ab}$  and  $\sigma_{\text{SC},ac}$ , determined from the data with the field applied along the  $c$  axis and in the kagome plane, respectively. When a magnetic field is applied along the  $c$  axis, superconducting screening currents will flow in the  $ab$  plane, whereas in the case of a magnetic field applied in-plane, the superconducting screening currents will flow along the  $c$  and  $a$  axes. Thus,  $\sigma_{\text{SC},ac}$  consists of both the in-plane and  $c$ -axis contributions. A two-step nature of the superconducting state with the onset of  $T_c \simeq 1.1 \text{ K}$  is clearly visible in the 5 mT data for both orientations of the magnetic field with respect to the  $c$  axis.

It is worth noticing that the step feature in the temperature dependence of the penetration depth that we observed for  $\text{KV}_3\text{Sb}_5$  is similar to the sudden decrease of the square root of the second moment of the field distribution at the vortex melting temperature in the cuprate high-temperature superconductor  $\text{Bi}_{2.15}\text{Sr}_{1.85}\text{CaCu}_2\text{O}_{8+\delta}$  (BSCCO)<sup>44</sup>. This process is thermally activated and caused by increased vortex mobility through a loosening of the inter- or intraplanar flux-line lattice correlations. This raises the question whether the two-step transition is related to the vortex lattice melting in  $\text{KV}_3\text{Sb}_5$ . We note several arguments against such a scenario. (1) In BSCCO, the step feature occurs not in low fields (10 mT, 20 mT) but only in higher fields at which vortex lattice melting takes place<sup>44</sup>. In low fields the effects of the thermal fluctuations of the vortex positions on the  $\mu$ SR linewidth become negligible, and a smooth temperature dependence of the linewidth is observed all the way up to  $T_c$  (ref. 44). In the case of  $\text{KV}_3\text{Sb}_5$ , the step-like feature is very well pronounced in 5 mT. With the application of 10 mT, the two-step transition becomes smoothed out and less pronounced. This is in contrast to what we expect in the scenario of vortex lattice melting. (2) The effect of the vortex lattice melting on the  $\mu$ SR line shape is to change its skewness from positive (ideal static lattice) to a negative value. Thus, vortex lattice melting is clearly reflected in the line shapes. In the case of  $\text{KV}_3\text{Sb}_5$ , the superconducting relaxation rate ( $\mu$ SR linewidth) is small due to the long penetration depth and the  $\mu$ SR line is described by a symmetric Gaussian line. Thus, it is difficult to check for the vortex lattice melting based on the shape of the field

distribution. However, we carried out such an analysis for the sister compound  $\text{CsV}_3\text{Sb}_5$  (ref. <sup>35</sup>), which exhibits a higher superconducting critical temperature and a higher width of the  $\mu\text{SR}$  line than the  $\text{KV}_3\text{Sb}_5$  sample. This enables us to describe the line shape more precisely. By analysing the asymmetric line shape of the field distribution and the skewness parameter as a function of temperature, we showed that the flux-line lattice in  $\text{CsV}_3\text{Sb}_5$  is well arranged in the superconducting state and it is slightly distorted only in the vicinity of  $T_c$ . However, no indication of vortex lattice melting was found in  $\text{CsV}_3\text{Sb}_5$  (ref. <sup>35</sup>). (3) We also note that the superconductors  $\text{AV}_3\text{Sb}_5$  are characterized by small superconducting anisotropy. The anisotropy of penetration depth for  $\text{CsV}_3\text{Sb}_5$  is 2–3, which is two orders of magnitude smaller than that for BSCCO. It is close to the values reported for Fe-based high-temperature superconductors, in which no vortex lattice melting transition is observed. Considering the above arguments, we think that the two-step temperature dependence of the low-field magnetic penetration depth in  $\text{KV}_3\text{Sb}_5$  is indeed due to multigap superconductivity with extremely small interband coupling<sup>34</sup>. The smearing of the step-like feature by increasing the magnetic field may be understood from the tendency of magnetic field to suppress one superconducting gap or by enhancing interband coupling with higher fields.

The temperature dependence of  $\lambda$  is sensitive to the topology of the superconducting gap: whereas in a fully gapped superconductor  $\Delta\lambda^{-2}(T) \equiv \lambda^{-2}(0) - \lambda^{-2}(T)$  vanishes exponentially at low  $T$ , in a nodal superconductor it vanishes as a power of  $T$ . To quantitatively analyse the temperature dependence of the penetration depth  $\lambda(T)$  (refs. <sup>42,45</sup>) for  $\text{KV}_3\text{Sb}_5$ , we use the empirical  $\alpha$ -model, which assumes that the gaps occurring in different bands, besides a common  $T_c$ , are independent of each other. The  $\lambda(T)$  in the applied field of 5 mT shows a well-pronounced two-step behaviour, as shown in Extended Data Fig. 7a. This suggests that at least two bands are involved in the superconductivity and that the interband coupling is extremely small, which is sufficient to have the same values of  $T_c$  for different bands but still shows the two-step temperature behaviour of the penetration depth<sup>34</sup>. With the application of 10 mT, the two-step transition becomes smoothed out and less pronounced. The results of the analysis for  $\mu_0 H = 10$  mT using the  $\alpha$ -model are presented in Extended Data Fig. 7b. We consider two different possibilities for the gap function: either a constant gap,  $\Delta_{0,i} = \Delta_i$ , or an angle-dependent  $f$ -wave gap of the form  $\Delta_{0,i} = \Delta_i \cos 3\varphi$ , which is appropriate for a triangular lattice, where  $\varphi$  is the polar angle around the Fermi surface. We note that the  $d$ -wave form  $\Delta_{0,i} = \Delta_i \cos 2\varphi$  makes no real sense on a lattice with three-fold rotational symmetry. The analysis certainly rules out a simple one-gap  $s$ -wave model as an adequate description of  $\lambda^{-2}(T)$  for  $\text{KV}_3\text{Sb}_5$ . The two-gap ( $s+s$ )-wave or two-gap ( $s+f$ )-wave models line up with the experimental data very well. Due to the lack of data points below 0.25 K, it is difficult to distinguish between ( $s+s$ )-wave and ( $s+f$ )-wave models and to give an estimate for the zero-temperature value of  $\lambda$ . We also observe a diamagnetic shift of about 1 G in the superconducting phase, as shown in Extended Data Fig. 7c, which indicates a  $T_c$  of  $\approx 1.1$  K, and furthermore supports the bulk nature of superconductivity in  $\text{KV}_3\text{Sb}_5$ .

The value of the in-plane penetration depth  $\lambda_{ab}$  at 0.3 K is found to be  $\lambda_{ab} \approx 877(20)$  nm. The value of the out-of-plane penetration depth, determined from  $\sigma_{\text{sc},c}$  (with superconducting screening currents flowing perpendicular to the kagome plane), is found to be  $\lambda_c \approx 730(20)$  nm. We note that these are the upper limits of  $\lambda_{ab}$  and  $\lambda_c$ , as they are obtained by assuming a 100% superconducting volume fraction. However, vortex lattice disorder increases the measured relaxation rate leading to an underestimation of the penetration depth. The unexpected observation of the slightly smaller penetration depth  $\lambda_c$  compared to  $\lambda_{ab}$  might therefore originate in a slightly stronger disorder of the vortex lattice when the field is applied in the kagome plane. Another possibility for the similar values of the penetration depths  $\lambda_{ab}$  and  $\lambda_c$  in  $\text{KV}_3\text{Sb}_5$  might be as follows. We have recently measured superconducting anisotropy in the related system  $\text{CsV}_3\text{Sb}_5$  (ref. <sup>35</sup>). The anisotropy

of the magnetic penetration depth is found to be around  $\gamma_\lambda \approx 3$ , which is a factor of three smaller than the anisotropy of the second magnetic critical field  $\gamma_{H_{c2}} \approx 9$  (ref. <sup>35</sup>). Such a difference was explained in terms of multiband superconductivity in comparison with well-established multigap superconductors (MgB<sub>2</sub>, Fe-based and so on). For  $\text{KV}_3\text{Sb}_5$ , the anisotropy of the second critical field is only  $\gamma_{H_{c2}} \approx 3$ . Assuming that both systems  $\text{CsV}_3\text{Sb}_5$  and  $\text{KV}_3\text{Sb}_5$  have similar superconducting mechanism, we expect the anisotropy of the penetration depth to be much smaller than 3, which makes this system exhibit an almost isotropic penetration depth.

### Analysis of the temperature dependence of $\lambda$

The temperature dependence of the penetration depth  $\lambda$  is particularly sensitive to the topology of the superconducting gap: whereas in a fully gapped superconductor,  $\Delta\lambda^{-2}(T) \equiv \lambda^{-2}(0) - \lambda^{-2}(T)$  vanishes exponentially at low  $T$ , in a nodal superconductor it vanishes as a power of  $T$ .  $\lambda(T)$  was calculated in the local (London) approximation ( $\lambda \gg \xi$ ) by using the following expression<sup>46</sup>:

$$\frac{\lambda^{-2}(T, \Delta_{0,i})}{\lambda^{-2}(0, \Delta_{0,i})} = 1 + \frac{1}{\pi} \int_0^{2\pi} \int_{\Delta(\tau, \varphi)}^{\infty} \left( \frac{\partial f}{\partial E} \right) \frac{E dE d\varphi}{\sqrt{E^2 - \Delta_i(T, \varphi)^2}}, \quad (5)$$

where  $f = [1 + \exp(E/k_B T)]^{-1}$  is the Fermi function,  $k_B$  is the Boltzmann constant,  $\varphi$  is the angle along the Fermi surface and  $\Delta_i(T, \varphi) = \Delta_{0,i} f(T/T_c) g(\varphi)$  ( $\Delta_{0,i}$  is the maximum gap value at  $T=0$ ). The temperature dependence of the gap is approximated by the expression  $f(T/T_c) = \tanh\{1.82[1.018(T_c/T - 1)]^{0.51}\}$ ;  $g(\varphi)$  describes the angular dependence of the gap and it is replaced by 1 for both an  $s$ -wave and an ( $s+s$ )-wave gap,  $|\cos(2\varphi)|$  for a  $d$ -wave gap and  $|\cos(3\varphi)|$  for an  $f$ -wave gap.

### Analysis of $\lambda(T)$ with a self-consistent approach

The  $\sigma_{\text{sc}}(T)$  data collected in the presence of a 50 G and 100 G field were analysed in the framework of the quasiclassical Eilenberger weak-coupling formalism, in which the temperature dependence of the gaps was obtained by solving the self-consistent coupled gap equations rather than using the phenomenological  $\alpha$ -model<sup>47-50</sup>, in which the latter considers a similar BCS-type temperature dependence for both gaps. The coupled gap equations as introduced by Kogan et al.<sup>51</sup> are

$$\begin{aligned} \delta_1 &= \frac{\Delta_1}{T_c} \frac{1}{2\pi t} \\ &= n_1 \lambda_{11} \delta_1 \\ &\sum_{n=0}^{\infty} \left[ S + \ln\left(\frac{1}{t}\right) - \left( \frac{1}{n+0.5} - \frac{1}{\sqrt{\delta_1^2 + (n+0.5)^2}} \right) \right] \\ &+ n_2 \lambda_{12} \delta_2 \sum_{n=0}^{\infty} \left[ S + \ln\left(\frac{1}{t}\right) - \left( \frac{1}{n+0.5} - \frac{1}{\sqrt{\delta_2^2 + (n+0.5)^2}} \right) \right], \end{aligned} \quad (6)$$

$$\begin{aligned} \delta_2 &= \frac{\Delta_2}{T_c} \frac{1}{2\pi t} \\ &= n_1 \lambda_{21} \\ &\delta_1 \sum_{n=0}^{\infty} \left[ S + \ln\left(\frac{1}{t}\right) - \left( \frac{1}{n+0.5} - \frac{1}{\sqrt{\delta_1^2 + (n+0.5)^2}} \right) \right] \\ &+ n_2 \lambda_{22} \delta_2 \sum_{n=0}^{\infty} \left[ S + \ln\left(\frac{1}{t}\right) - \left( \frac{1}{n+0.5} - \frac{1}{\sqrt{\delta_2^2 + (n+0.5)^2}} \right) \right], \end{aligned} \quad (7)$$

where

$$S = \frac{n_1\lambda_{11} + n_2\lambda_{22} - \sqrt{(n_1\lambda_{11} - n_2\lambda_{22})^2 + 4n_1n_2\lambda_{12}^2}}{2n_1n_2(\lambda_{11}\lambda_{22} - \lambda_{12}^2)}, \quad (8)$$

and  $t = T/T_c$  is the reduced temperature.  $n_1$  and  $n_2$  represent the partial density of states for the corresponding bands at the Fermi level.  $\lambda_{11}$  ( $\lambda_{22}$ ) and  $\lambda_{12}$  ( $\lambda_{21}$ ) are the strengths of the intraband and the interband coupling, respectively. The two interband coupling strengths are equal, that is,  $\lambda_{12} = \lambda_{21}$  in the notation of Kogan et al. The temperature variation of  $\Delta_1(T)$  and  $\Delta_2(T)$  obtained after solving the above-mentioned coupled gap equations are then used to evaluate the temperature dependence of the normalized inverse-square magnetic penetration depth  $\lambda_v^{-2}(T)/\lambda_v^{-2}(0)$ , which in turn directly relates to the superfluid densities  $\rho_v(T)$  for the two bands, by using the expression

$$\rho_v(T) = \frac{\lambda_v(T)^{-2}}{\lambda_v(0)^{-2}} = \delta_v^2 \sum_{n=0}^{\infty} \left[ \delta_v^2 + (n + 0.5)^2 \right]^{-\frac{3}{2}}, \quad (9)$$

where  $\nu = 1, 2$  are the band indices.

The total superfluid density is then extracted by using the known temperature variations of  $\rho_1(T)$  and  $\rho_2(T)$  through the following expression:

$$\rho(T) = \gamma\rho_1(T) + (1 - \gamma)\rho_2(T), \quad (10)$$

where  $\gamma$  is the weighting factor for the contribution of superconducting states with the larger gap  $\Delta_1$ . A detailed description of the model can be found in ref.<sup>52</sup>.

The results of these analyses are shown in Extended Data Fig. 8a–c. Our numerical analysis shows that the two-step transition in  $\sigma_{sc}(T)$  at 10 mT requires the interband coupling constant to be small, with a value of 0.005. For 5 mT data, the interband coupling constant was found to be 0.001, which is factor of five smaller than that estimated for 10 mT. This explains why the step-like feature is smoothed out in 10 mT. The small values of interband coupling constants imply that the band(s), in which the large and the small superconducting energy gaps are open, become only weakly coupled. One important point is that if we assume the maximum gap-to- $T_c$  ratio to be 3.75 (BCS value), which is a limitation of the model, then one cannot reproduce the sharp step-like feature in  $\sigma_{sc}(T)$ . However, considering this limitation of model, then the data are well explained by a large value of  $2\Delta/k_B T_c = 7$ . Our observation of a two-step behaviour of penetration depth in the system  $KV_3Sb_5$  with single  $T_c$  is consistent with two-gap superconductivity with very weak interband coupling and a large value of  $2\Delta/k_B T_c = 7$ .

## Data availability

All relevant data are available from the authors. Alternatively, the data can be accessed through the data base at the following link: <http://musruser.psi.ch/cgi-bin/SearchDB.cgi>.

41. Amato, A. et al. The new versatile general purpose surface-muon instrument (GPS) based on silicon photomultipliers for  $\mu$ SR measurements on a continuous-wave beam. *Rev. Sci. Instrum.* **88**, 093301 (2017).
42. Suter, A. and Wojek, B. M. Musrfit: a free platform-independent framework for  $\mu$ SR data analysis. *Phys. Procedia* **30**, 69 (2012).

43. Kiesel, M. L. & Thomale, R. Sublattice interference in the kagome Hubbard model. *Phys. Rev. B* **86**, 121105 (2012).
44. Lee, S. L. et al. Evidence for two-dimensional thermal fluctuations of the vortex structure in  $Bi_{1.85}Sr_{1.05}CaCu_2O_{8+\delta}$  from muon spin rotation experiments. *Phys. Rev. Lett.* **75**, 922 (1995).
45. Guguchia, Z. et al. Signatures of the topological  $s^+$  superconducting order parameter in the type-II Weyl semimetal  $T_x$ -MoTe<sub>2</sub>. *Nat. Commun.* **8**, 1082 (2017).
46. Brandt, E. H. Flux distribution and penetration depth measured by muon spin rotation in high- $T_c$  superconductors. *Phys. Rev. B* **37**, 2349 (1988).
47. Bouquet, F. et al. Phenomenological two-gap model for the specific heat of  $MgB_2$ . *Europhys. Lett.* **56**, 856 (2001).
48. Prozorov, R. & Giannetta, R. W. Magnetic penetration depth in unconventional superconductors. *Supercond. Sci. Technol.* **19**, R41 (2006).
49. Khasanov, R. et al. Experimental evidence for two gaps in the high-temperature  $La_{1.83}Sr_{0.17}CuO_4$  superconductor. *Phys. Rev. Lett.* **98**, 057007 (2007).
50. Khasanov, R. et al. SrPt<sub>3</sub>P: a two-band single-gap superconductor. *Phys. Rev. B* **90**, 140507(R) (2014).
51. Kogan, V. G. London approach to anisotropic type-II superconductors. *Phys. Rev. B* **24**, 1572 (1981).
52. Gupta, R. et al. Self-consistent two-gap approach in studying multi-band superconductivity in  $NdFeAsO_{0.65}F_{0.35}$ . *Front. Phys.* **8**, 2 (2020).

**Acknowledgements** The  $\mu$ SR experiments were carried out at the Swiss Muon Source ( $\mu$ S) Paul Scherrer Institute, Villigen, Switzerland. The magnetization measurements were carried out on the MPMS device of the Laboratory for Multiscale Materials Experiments, Paul Scherrer Institute, Villigen, Switzerland (SNSF grant no. 206021\_139082). Z.G. acknowledges the useful discussions with R. Scheuermann and A. Amato. Z.G., C.M.III and D.D. thank C. Baines for the technical assistance during DOLLY experiments. M.Z.H. acknowledges visiting scientist support from IQIM at the California Institute of Technology. Experimental and theoretical work at Princeton University was supported by the Gordon and Betty Moore Foundation (GBMF4547 and GBMF9461; M.Z.H.) and the material characterization is supported by the US Department of Energy under the Basic Energy Sciences programme (grant no. DOE/BES DE-FG-02-05ER46200). The theory work at Rice has primarily been supported by the US Department of Energy, BES under award no. DE-SC0018197 and has also been supported by the Robert A. Welch Foundation grant no. C-1411 (Q.S.). The work at Rice university is also supported by US Department of Energy, BES under Grant No. DE-SC0012311 (P.D.). This work is also supported by the Beijing Natural Science Foundation (grant no. Z180008, Z200005), the National Key Research and Development Program of China (grant no. 2017YFA0302900, Y2018YFE0202600) and the National Natural Science Foundation of China (grant no. U2032204). The work of R.G. was supported by the Swiss National Science Foundation (SNF grant no. 200021\_175935). T.N. acknowledges funding from the European Research Council (ERC) under the European Union's Horizon 2020 research and innovation program (ERC-StG-Neupert-757867-PARATOP). H. M. was sponsored by the US Department of Energy, Office of Science, Basic Energy Sciences, Materials Sciences and Engineering Division. R.T. was supported by the Deutsche Forschungsgemeinschaft (DFG, German Research Foundation) through Project-ID 258499086-SFB1170 and by the Wurzburg-Dresden Cluster of Excellence on Complexity and Topology in Quantum Matter-ct.qmat Project-ID 390858490-EXC 2147.

**Author contributions** Z.G., Y.-X.J. and M.Z.H. conceived the study. Z.G. supervised the project. Sample growth and single-crystal X-ray diffraction experiments were carried out by H. Liu and Y.S. Magnetization and Laue X-ray diffraction experiments were performed by C.M.III, Z.G., M.M. and H.C.L.  $\mu$ SR experiments and corresponding discussions were carried out by Z.G., C.M.III, D.D., R.G., R.K., H.Luet., J.J.C., J.-X.Y., Y.-X.J., M.Z.H., X.W., P.D., Q.S., H.M., R.T. and T.N.  $\mu$ SR data analysis was undertaken by Z.G. and C.M.III, with contributions from R.K., H.L., D.D. and R.G. STM experiments were performed by J.-X.Y., Y.-X.J. and M.Z.H. Figure development and the writing of the paper were carried out by Z.G. and C.M.III, with contributions from J.-X.Y., H.Luet. and M.Z.H. All authors discussed the results, interpretation and conclusion.

**Competing interests** The authors declare no competing interests.

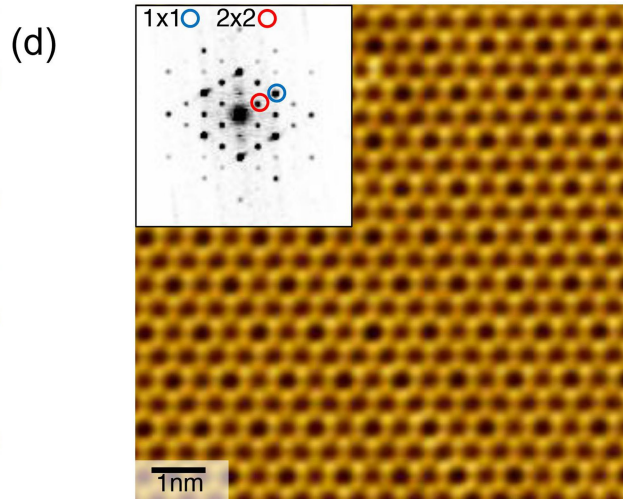
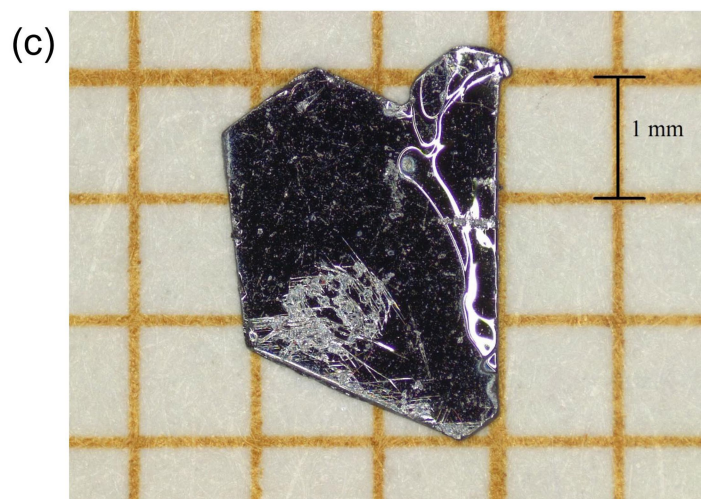
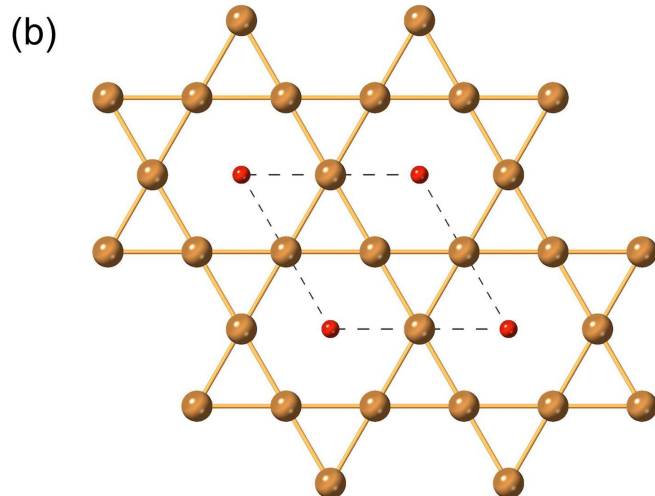
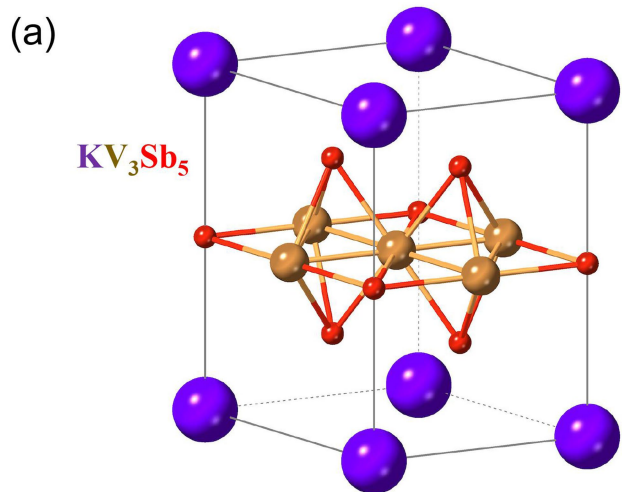
## Additional information

**Supplementary information** The online version contains supplementary material available at <https://doi.org/10.1038/s41586-021-04327-z>.

**Correspondence and requests for materials** should be addressed to M. Z. Hasan or Z. Guguchia.

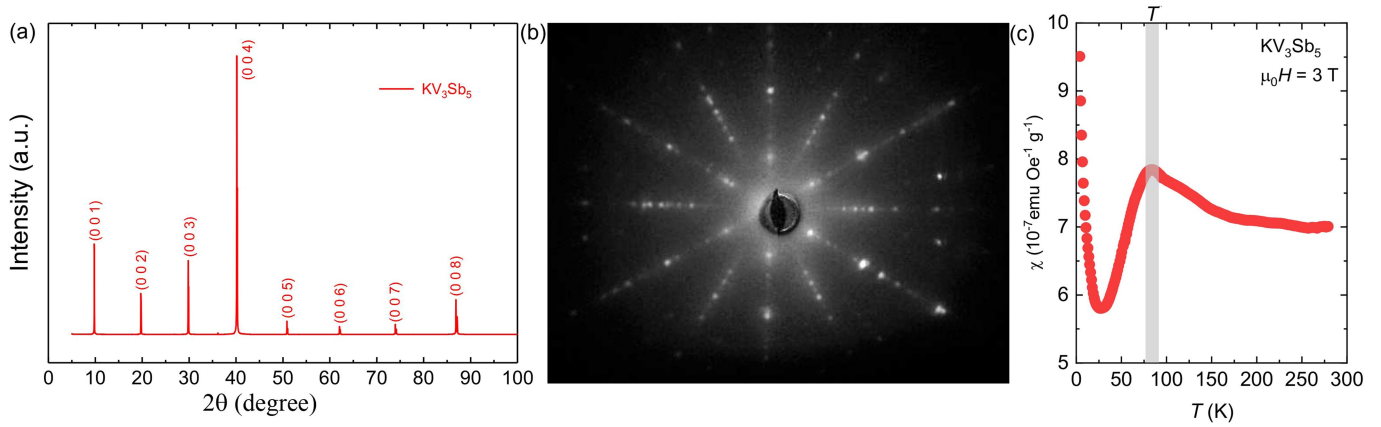
**Peer review information** Nature thanks Victor Yakovenko and the other, anonymous, reviewer(s) for their contribution to the peer review of this work.

**Reprints and permissions information** is available at <http://www.nature.com/reprints>.



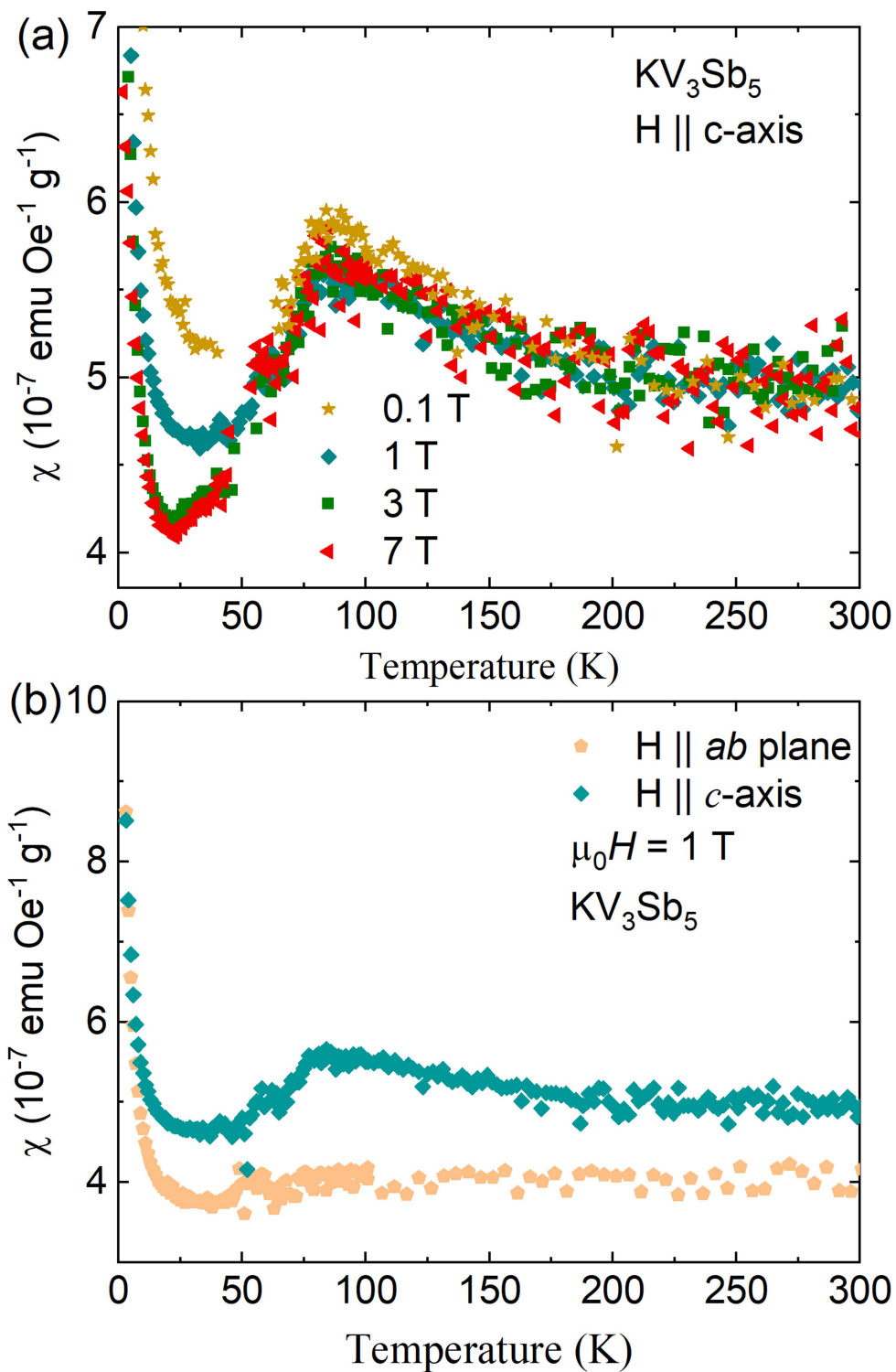
**Extended Data Fig. 1 | Crystal structure of  $KV_3Sb_5$ .** Three dimensional representation (a) and top view (b) of the atomic structure of  $KV_3Sb_5$ . In panel (c) is displayed an optical microscope image of a  $3 \times 2 \times 0.2$  mm single crystal of

$KV_3Sb_5$  on millimeter paper, with the scale shown. The hexagonal symmetry is immediately apparent. (d) Scanning Transmission Microscope (STM) image of the V kagome lattice from a cryogenically cleaved sample.



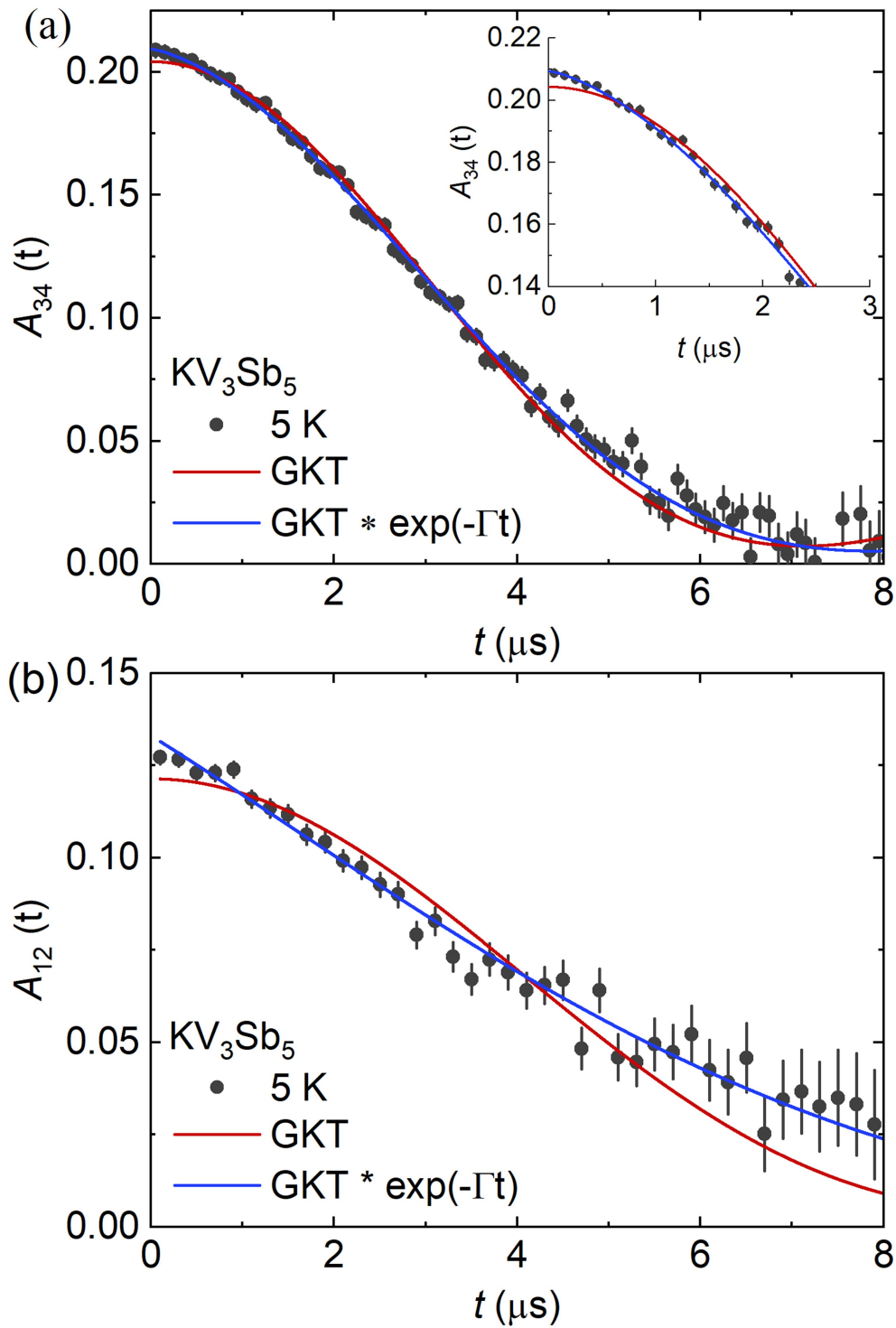
**Extended Data Fig. 2 | Single Crystal X-Ray Diffraction for  $KV_3Sb_5$ .** (a) X-ray diffraction image for  $KV_3Sb_5$  recorded at 300 K. The well-defined peaks are labeled with their crystallographic indices. No second phase has been detected. (b) Laue X-ray diffraction image of the single crystal sample  $KV_3Sb_5$ ,

oriented with the  $c$ -axis along the beam. (c) The temperature dependence of magnetic susceptibility of  $KV_3Sb_5$  above 1.8 K. It shows an anomaly at  $T \approx 80$  K, coinciding with emergence of a charge order.



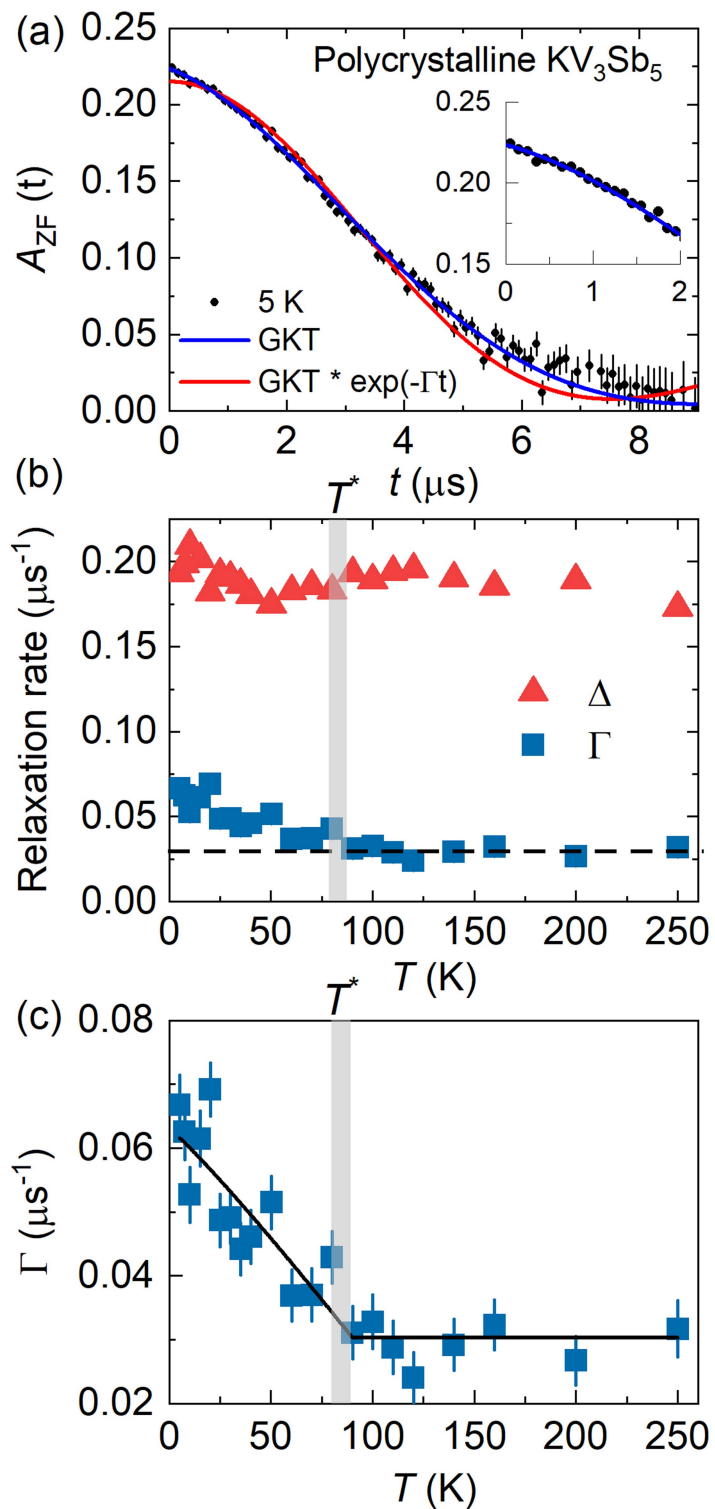
**Extended Data Fig. 3 | Anisotropic magnetic response across charge order temperature in the single crystalline sample of KV<sub>3</sub>Sb<sub>5</sub>.** (a) The temperature dependence of magnetic susceptibility for KV<sub>3</sub>Sb<sub>5</sub> measured at various

magnetic fields applied parallel to the c-axis. (b) The temperature dependence of magnetic susceptibility for KV<sub>3</sub>Sb<sub>5</sub> measured in the field of 1 T, applied both parallel to the kagome plane and parallel to the c-axis.



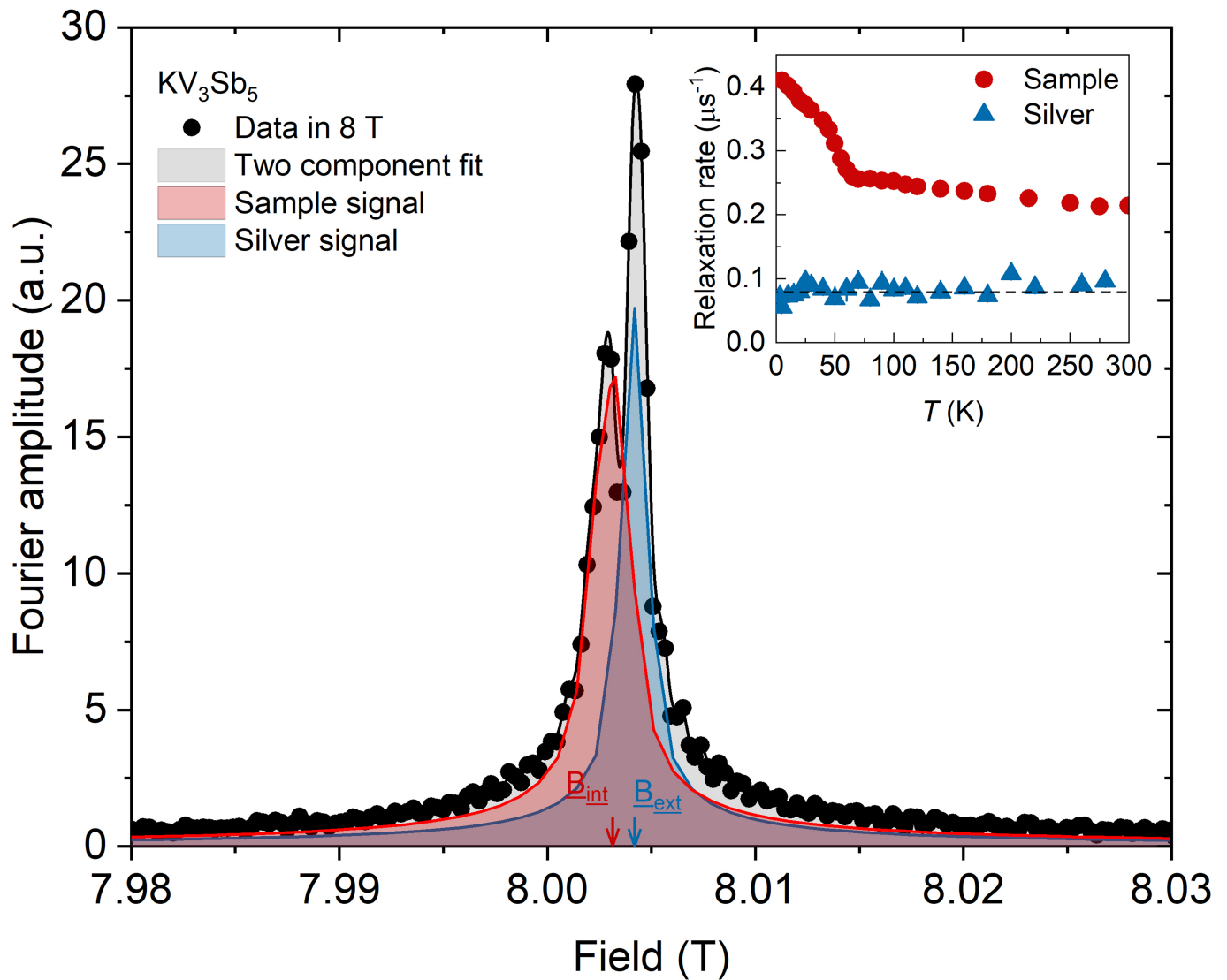
**Extended Data Fig. 4 | Zero-field  $\mu\text{SR}$  experiment for the single crystalline sample of  $\text{KV}_3\text{Sb}_5$ .** The ZF  $\mu\text{SR}$  time spectra for  $\text{KV}_3\text{Sb}_5$ , obtained at  $T = 5$  K from detectors 3 & 4 and 2 & 1. The solid curves represent fits to the recorded time

spectra, using only Gaussian Kubo Toyabe (GKT) function (red) and the one with an additional exponential  $\exp(-\Gamma t)$  term (blue). The inset shows the low time part of the spectrum.



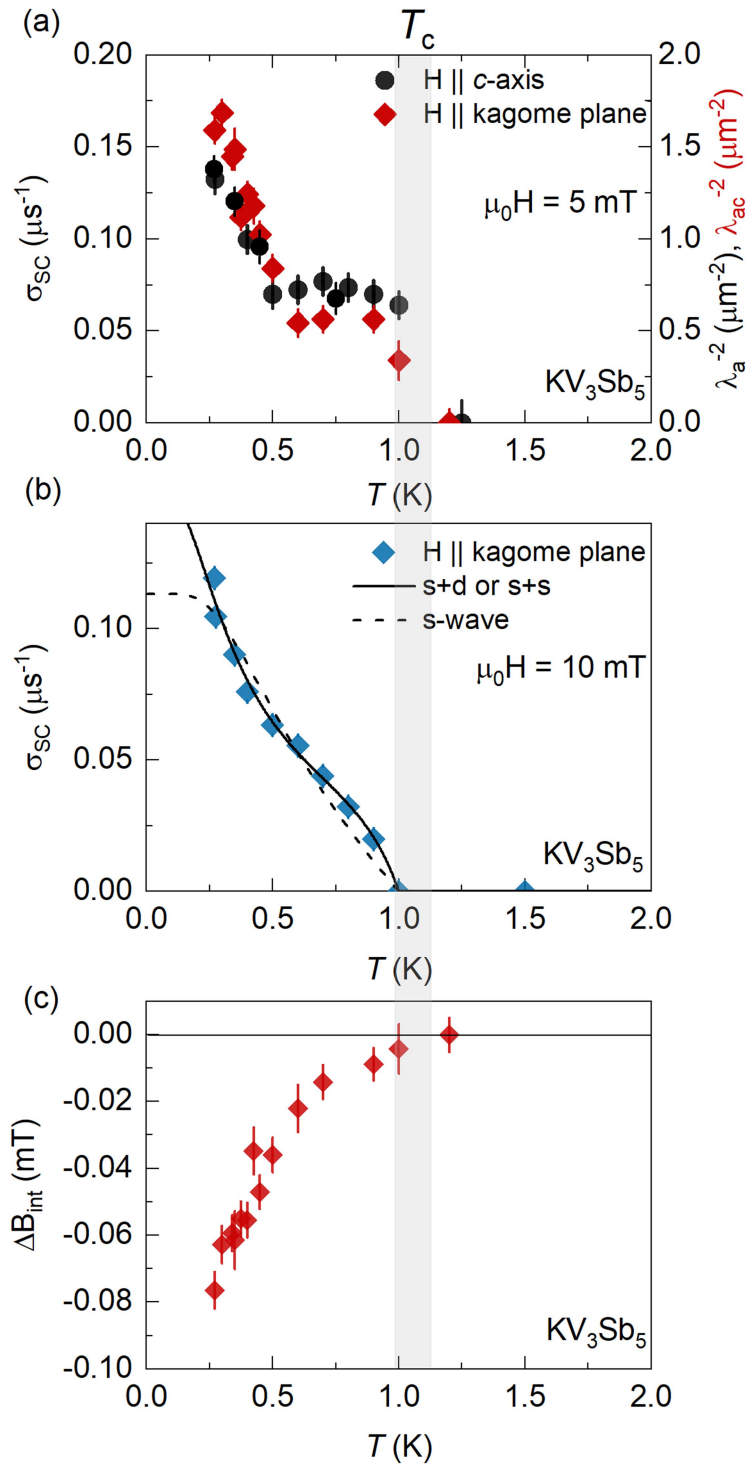
**Extended Data Fig. 5 | Zero-field  $\mu$ SR experiment for the polycrystalline sample of  $KV_3Sb_5$ .** The ZF  $\mu$ SR time spectra for the polycrystalline sample of  $KV_3Sb_5$ , obtained at  $T=5$  K. The solid curves represent fits to the recorded time

spectra, using only Gaussian Kubo Toyabe (GKT) function (red) and the one with an additional exponential  $\exp(-\Gamma t)$  term (blue). The inset shows the low time part of the spectrum.



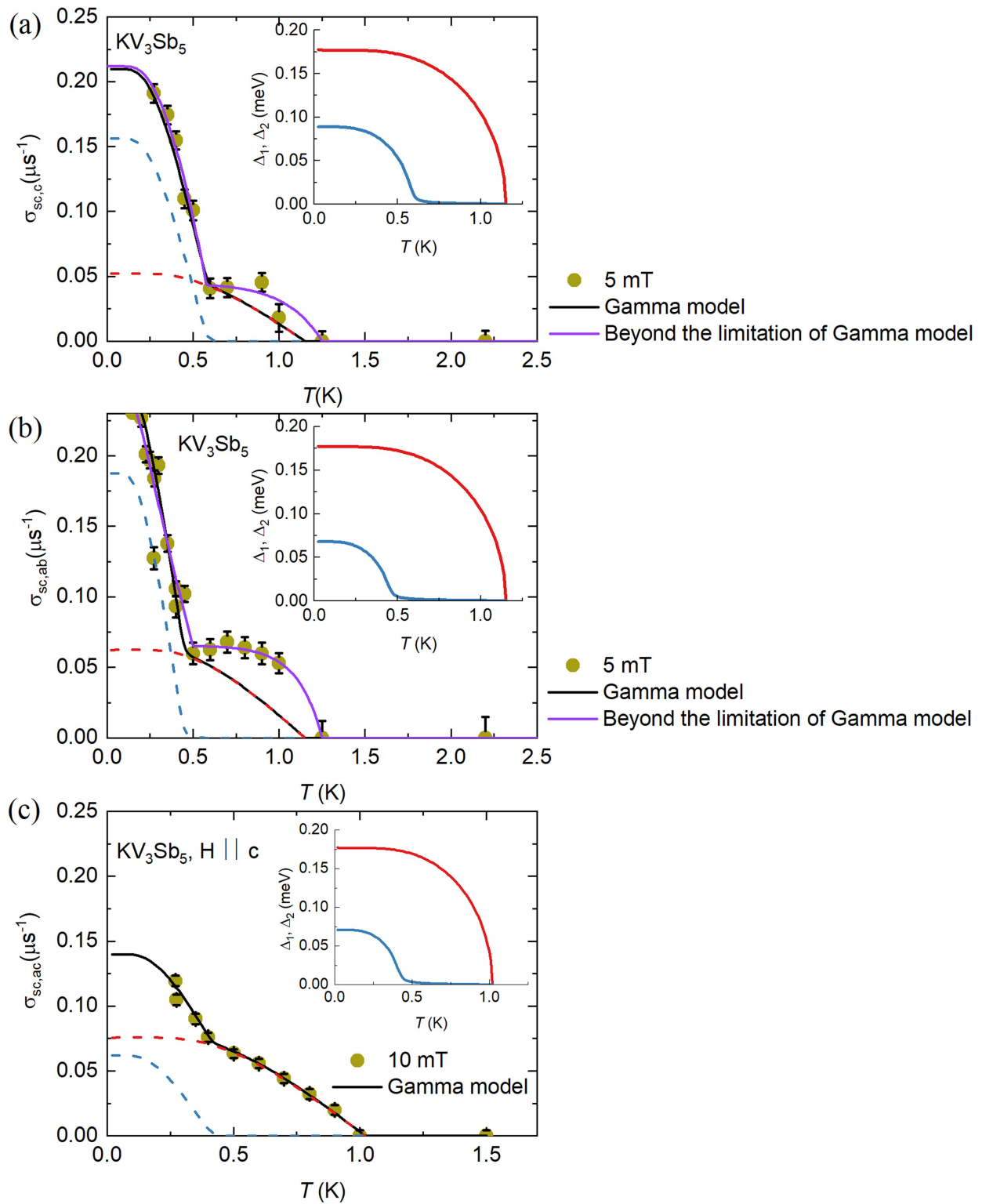
**Extended Data Fig. 6 | High-field  $\mu$ SR experiment for  $KV_3Sb_5$ .** Fourier transform for the  $\mu$ SR asymmetry spectra of  $KV_3Sb_5$  at 5 K for the applied field of  $\mu_0 H = 8$  T. The black solid line represents the fit to the data using the two component signal. Red and blue solid lines show the signals arising from the

sample and the silver sample holder (majority), respectively. The inset shows the temperature dependences of the muon spin relaxation rates arising from the sample and the silver sample holder.



**Extended Data Fig. 7 | Superconducting gap symmetry in  $\text{KV}_3\text{Sb}_5$ .** (a) The SC muon depolarization rates  $\sigma_{SC,ab}$ , and  $\sigma_{SC,ac}$  as well as the inverse squared magnetic penetration depth  $\lambda_{ab}^{-2}$  and  $\lambda_{ac}^{-2}$  as a function of temperature, measured in 5 mT, applied parallel and perpendicular to the kagome plane. (b) The SC muon depolarization rate  $\sigma_{SC,ac}$ , measured in 10 mT, applied parallel

to the kagome plane. The solid line represents the indistinguishable 2-gap  $s$ -wave and  $s+d$  wave model. The error bars represent the s.d. of the fit parameters. (c) Temperature dependence of the difference between the internal field  $\mu_0 H_{SC}$  measured in the SC state and the one measured in the normal state  $\mu_0 H_{NS}$  at  $T = 5$  K for  $\text{KV}_3\text{Sb}_5$ .



**Extended Data Fig. 8 | A self-consistent approach for a two-band superconductor in  $\text{KV}_3\text{Sb}_5$ .** The SC muon depolarization rates  $\sigma_{\text{sc},c}$  (a), and  $\sigma_{\text{sc},ab}$  (b) as a function of temperature, measured in 5 mT, applied perpendicular and parallel to the kagome plane. (c) The SC muon depolarization rate  $\sigma_{\text{sc},ac}$ , measured in 10 mT, applied parallel to the kagome plane. The solid black and purple lines are the theoretical curves obtained within the framework of

self-consistent approach for a two-band superconductor described in the text. The red and the blue dashed lines correspond to the contribution of the large and the small superconducting gaps to the total superfluid density, solid black lines. The insets show the temperature dependences of the large  $\Delta_1$  and the small  $\Delta_2$ .

Extended Data Table 1 | Atomic positions

Atomic Positions						
Atom	Wyckhoff Positions	x	y	z	$U_{eq}/\text{\AA}^2$	Occ
Sb <sub>01</sub>	1a	1	1	0	0.16	1
Sb <sub>02</sub>	4h	2/3	1/3	0.25381	0.019	1
V <sub>01</sub>	3f	1/2	1/2	0	0.015	1
K <sub>01</sub>	1b	1	0	1/2	0.045	0.977

Summary of the atomic positions obtained from fitting to the diffraction data.

Crystallographic Data	
Chemical Formula	$K_{0.98}V_3Sb_5$
Formula Weight	799.81 $\frac{g}{mol}$
Crystal System	hexagonal
Space Group	$P6/mmm$
$a$	5.4831(3) Å
$c$	8.9544(9) Å
$\alpha$	90°
$\gamma$	120°
$Z$	1 Å
Cell Volume	233.14(3) Å <sup>3</sup>
Density (calculated)	5.697 $\frac{g}{cm^3}$
Temperature	273(2) K
Wavelength	Mo $K_{\alpha}$ ( $\lambda = 0.71073$ Å)
$\theta$ Range	2.27° to 36.15°
Data Collection	
Diffractometer	Bruker D8 Venture
Index Ranges	$-9 \leq h \leq 9$ $-9 \leq k \leq 9$ $-14 \leq l \leq 14$
Reflections Collected	7207
Independent Reflections	278 [ $R_{int} = 0.0380$ ]
Absorption Coefficient	17.469 mm <sup>-1</sup>
Structure Solution Tech.	Direct methods
Structure Solution Prog.	SHELX-2014/5 (Sheldrick,2014)
Refinement	
Refinement Method	Full-matrix least-squares on $F^2$
Refinement Program	SHELX-2018/3 (Sheldrick,2018)
Function Minimized	$\Sigma w(F_o^2 + F_c^2)^2$
Data	278 reflections (271 final)
Parameters	13 parameters
Restraints	0 restraints
Goodness-of-fit on $F^2$	1.233
Final $R$ Indices	$I \leq \sigma(I)$ $R_1=0.0162$ , $wR_2=0.039$ all data; $R_1=0.0171$ , $wR_2=0.039$
Weighting Scheme	$w = \frac{1}{\sigma^2(F_o^2) + (0.0130P)^2 + 0.4869P}$ where $P = (F_o^2 + 2F_c^2)/3$
Extinction Coefficient	0.0050(10)
$\Delta\rho_{Max}$ and $\Delta\rho_{sMin}$	1.259 eÅ <sup>-3</sup> and -0.481 eÅ <sup>-3</sup>
R.M.S. Dev. from Mean	0.164 eÅ <sup>3</sup>

Summary of the crystallographic refinement, and data collection information from the refinements to the single crystal X-ray diffraction data.